



Origin of negative magnetization phenomena in $(\text{Tm}_{1-x}\text{Mn}_x)\text{MnO}_3$: A neutron diffraction studyAndreas Dönni ¹, Vladimir Y. Pomjakushin,² Lei Zhang,^{3,4} Kazunari Yamaura,^{3,4} and Alexei A. Belik ^{3,*}¹*International Center for Materials Nanoarchitectonics (WPI-MANA), National Institute for Materials Science (NIMS), Namiki 1-1, Tsukuba, Ibaraki 305-0044, Japan*²*Laboratory for Neutron Scattering and Imaging (LNS), Paul Scherrer Institut, 5232 Villigen PSI, Switzerland*³*Research Center for Functional Materials, National Institute for Materials Science (NIMS), Namiki 1-1, Tsukuba, Ibaraki 305-0044, Japan*⁴*Graduate School of Chemical Sciences and Engineering, Hokkaido University, North 10 West 8, Kita-ku, Sapporo, Hokkaido 060-0810, Japan*

(Received 15 December 2019; accepted 3 February 2020; published 28 February 2020)

$(\text{Tm}_{1-x}\text{Mn}_x)\text{MnO}_3$ solid solutions were synthesized at a high pressure of 6 GPa and a high temperature of about 1570–1670 K for 2 h for $x = 0, 0.1, 0.2,$ and 0.3 . Magnetic, dielectric, and neutron diffraction measurements revealed that the introduction of magnetic Mn^{2+} cations into the A site leads to an incommensurate spin structure for $x = 0.1$ and to a ferrimagnetic structure for $x \geq 0.2$. Commensurate magnetic structures have a much larger correlation length (~ 400 nm for $x = 0$, ~ 600 nm for $x = 0.3$) than the incommensurate magnetic structure (~ 12 nm for $x = 0.1$). The presence of Tm^{3+} and Mn^{2+} (with different sizes) at the A site causes significant microstrain effects along the a direction which are absent for $x = 0$ and get stronger with increasing x . Magnetic ordering occurs at the Néel temperature $T_N = 37$ K ($x = 0.1$) and at the ferrimagnetic Curie temperatures $T_C = 75$ K ($x = 0.2$) and $T_C = 104$ K ($x = 0.3$). Ordering of magnetic Mn moments triggers short-range order (for $x = 0.1$) and long-range order (for $x \geq 0.2$) of the Tm^{3+} cations at the same temperature—an unusual situation in perovskite materials with a simple GdFeO_3 -type $Pnma$ structure. For $x = 0.1$, long-range IC magnetic order [with propagation vector $\mathbf{k} = (k_0, 0, 0)$ and $k_0 \approx 0.40$] of Mn^{3+} and Mn^{4+} cations at the B site coexists with short-range order of Tm^{3+} and Mn^{2+} moments at the A site. Short-range order is induced at the Néel temperature $T_N = 37$ K, increases towards an additional specific heat anomaly at $T = 4$ K, and remains at lower temperature. The ferrimagnetic structure [with propagation vector $\mathbf{k} = (0, 0, 0)$] consists of ferromagnetically ordered Mn^{3+} and Mn^{4+} cations at the B site which are coupled antiferromagnetically with ordered Mn^{2+} moments at the A site. Tm^{3+} moments adopt a zigzag magnetic structure which contains a macroscopic ferromagnetic moment that aligns with the direction of the ordered Mn^{2+} moments. Towards low temperature, the ordered Tm^{3+} moments strongly increase and overcome the saturated magnetic Mn moments at the B site, and this behavior results in the observation of magnetization reversal or negative magnetization phenomena with a compensation temperature of about 15 K at small magnetic fields in the $x = 0.2$ and 0.3 samples. This is a classical mechanism of the magnetization reversal effects for ferrimagnets.

DOI: [10.1103/PhysRevB.101.054442](https://doi.org/10.1103/PhysRevB.101.054442)**I. INTRODUCTION**

Perovskite-structure oxides, ABO_3 , usually have nonmagnetic cations at the A site (for example, A = Li, Na, Ca, Sr, and Ba) and nonmagnetic or magnetic rare-earth (R) cations. The B site is usually occupied by cations of magnetic or nonmagnetic $3d$ - $5d$ transition metals and other nonmagnetic cations, such as Mg^{2+} , Al^{3+} , Ga^{3+} , and so on [1,2]. Even in situations when both A and B sites are occupied by magnetic cations, the interaction between the A and B sublattices is very weak. This fact is manifested in very different magnetic transition temperatures of the B and R sublattices. For example, Fe^{3+} cations at the B site are ordered at $T_{N,\text{Fe}} = 620$ – 740 K in RFeO_3 , while (some) magnetic R^{3+} cations at the A site are ordered at $T_{N,R} = 2$ – 8 K [3]. Cr^{3+} cations at the B site are ordered at $T_{N,\text{Cr}} = 110$ – 280 K in RCrO_3 , while (some) magnetic R^{3+} cations at the A site are ordered

at $T_{N,R} = 2$ – 10 K [3]. A more complex picture takes place in RMnO_3 manganites, where there are two magnetic transitions associated with the Mn^{3+} at the B site (for R = Gd-Lu and Y) [4], and R^{3+} cations order at relatively higher temperatures in comparison with RFeO_3 and RCrO_3 , for example, $T_{N,\text{Mn}} = 73$ K and $T_{N,\text{Nd}} = 15$ K in NdMnO_3 [5], and $T_{N,\text{Mn}} = 47.5$ K and $T_{N,\text{Ho}} \approx 20$ K in HoMnO_3 [6]. In o-TmMnO_3 , a parent compound of this study [7], an incommensurate (IC) spin structure at the Mn site (B site) appears below $T_{N1,\text{Mn}} = 42$ K and locks into a commensurate noncollinear E -type structure below $T_{N2,\text{Mn}} = 30$ – 32 K with the appearance of spin-induced ferroelectricity. Tm^{3+} cations at the A site spontaneously order at a much lower temperature below $T_{N3,\text{Tm}} = 4$ K.

Some $3d$ transition metals can be “doped” into the A site of perovskites. The appearance of $3d$ transition metals at the A site significantly enriches magnetic and related properties of such perovskites [8]. Depending on the nature of $3d$ transition metals and the amount of doping different situations can be realized. 100% of doping gives, for example, MnVO_3

*Corresponding author: alexei.belik@nims.go.jp

[9] and $\text{Mn}_2\text{FeSbO}_6$ [10] (which demonstrate incommensurate antiferromagnetic Mn^{2+} spin order), $\text{Mn}_2\text{MnReO}_6$ [11], and $\text{Mn}_2\text{FeReO}_6$ (which shows high ferrimagnetic transition temperature and giant and switchable magnetoresistance) [12,13]. They all crystallize in simple perovskite structures—derivatives of the GdFeO_3 -type structure.

75% of doping can result in the so-called A-site-ordered quadruple perovskites with a general composition of $\text{AA}'_3\text{B}_4\text{O}_{12}$, where a square-planar A' site is usually occupied by Cu^{2+} , Mn^{2+} , and Mn^{3+} [14]. The interaction between $3d$ transition metals located at the A' and B sites can be strong resulting in simultaneous magnetic ordering of cations at these sites, for example, in $\text{AMn}_7\text{O}_{12}$ ($A = \text{Cd}, \text{Ca}, \text{Sr}, \text{and Pb}$) [15], $\text{RMn}_7\text{O}_{12}$ [16], and $\text{RCu}_3\text{Mn}_4\text{O}_{12}$ [17]. But the A sublattice still shows weaker coupling if it is occupied by magnetic rare-earth cations. For example, Mn^{3+} cations at both A' and B sites are ordered at $T_{N,\text{Mn}} = 85$ K in $\text{NdMn}_7\text{O}_{12}$, while Nd^{3+} cations at the A site are ordered at $T_{N,\text{Nd}} = 8.5$ K [16]; $T_{N,\text{Mn}} = 108$ K in $\text{DyMn}_7\text{O}_{12}$, while $T_{N,\text{Dy}} = 8.5$ K [18]; $T_{N,\text{Mn}/\text{Cu}} = 395$ K in $\text{TbCu}_3\text{Mn}_4\text{O}_{12}$, while $T_{N,\text{Tb}} \sim 60$ K [17].

50% of doping can result in the so-called A-site columnar-ordered quadruple perovskites with a general composition of $\text{A}_2\text{A}'\text{A}''\text{B}_4\text{O}_{12}$ [19], where a square-planar A' site is usually occupied by Cu^{2+} , Mn^{2+} , and Mn^{3+} , and a tetrahedral A'' site by Mn^{2+} . Mn cations at three A' , A'' , and B sites can order at the same time, for example, at $T_{N,\text{Mn}} = 74$ K in TmMn_3O_6 [20] and at $T_{N,\text{Mn}} = 76$ K in NdMnMnSbO_6 [21], while rare-earth cations at the A site usually order at lower temperatures: $T_{N,\text{Tm}} = 28$ K in TmMn_3O_6 and at $T_{N,\text{Nd}} = 42$ K in NdMnMnSbO_6 . Note that in this subfamily of perovskites, the $T_{N,R}/T_{N,\text{Mn}}$ ratio is noticeably higher than that of other subfamilies reported so far, and it can even reach unity. For example, all magnetic cations order at the same temperature ($T_{N,\text{Pr}} = T_{N,\text{Mn}} = 62$ K) in PrMnMnSbO_6 [22].

75%, 50%, and other doping levels can also produce disordered arrangements of cations at the A site and simple perovskite structures. We have recently found the formation of $(\text{R}_{1-x}\text{Mn}_x)\text{MnO}_3$ solid solutions for $\text{R} = \text{Er-Lu}$ with the GdFeO_3 -type $Pnma$ structure [23,24]. Magnetic properties of $(\text{R}_{1-x}\text{Mn}_x)\text{MnO}_3$ were significantly modified in comparison with undoped RMnO_3 perovskites due to the presence of magnetic Mn^{2+} cations at the A sites even at the doping level of 20%, for example, ferrimagnetic structures were realized in $(\text{Lu}_{1-x}\text{Mn}_x)\text{MnO}_3$ for $0.2 \leq x \leq 0.4$ and magnetization reversal or negative magnetization effects [25] were observed in $(\text{Tm}_{0.667}\text{Mn}_{0.333})\text{MnO}_3$.

In this work we report results of our detailed investigation of $(\text{Tm}_{1-x}\text{Mn}_x)\text{MnO}_3$ solid solutions. A negative magnetization effect was observed for $0.2 \leq x \leq 0.333$. Neutron diffraction measurements for the $x = 0.3$ sample allowed us to explain this effect by a classical model with two magnetic sublattices having different temperature dependencies of magnetization.

II. EXPERIMENT

$(\text{Tm}_{1-x}\text{Mn}_x)\text{MnO}_3$ solid solutions were synthesized from stoichiometric mixtures of Mn_2O_3 and Tm_2O_3 (99.9%) for $x = 0.1, 0.2,$ and 0.3 . The mixtures were placed in Pt cap-

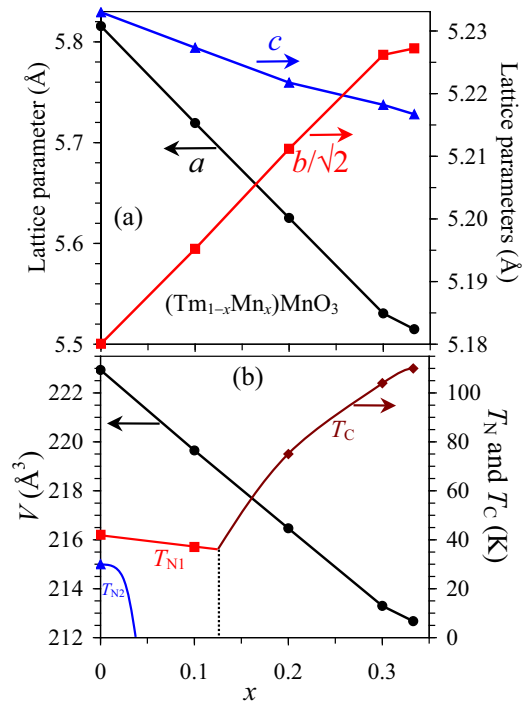


FIG. 1. Compositional dependence of (a) the orthorhombic lattice parameters (a , b , and c) and (b) unit cell volume and magnetic transition temperatures in a form of a phase diagram in the $(\text{Tm}_{1-x}\text{Mn}_x)\text{MnO}_3$ solid solutions with $0 \leq x \leq 0.33$. T_{N1} and T_{N2} are antiferromagnetic Néel temperatures and T_C is the ferrimagnetic Curie temperature.

sules and treated at a high pressure of 6 GPa and a high temperature of about 1670 K for 2 h (heating time to the synthesis temperature was 10 min) in a belt-type high-pressure apparatus. After the heat treatments, the samples were quenched to room temperature (RT), and the pressure was slowly released. All the samples obtained were black pellets (quite friable in some cases). Several batches of $(\text{Tm}_{0.9}\text{Mn}_{0.1})\text{MnO}_3$ (with the total weight of 2.056 g) and $(\text{Tm}_{0.7}\text{Mn}_{0.3})\text{MnO}_3$ (with the total weight of 2.807 g) were prepared for neutron diffraction. Single-phase Mn_2O_3 was prepared from commercial MnO_2 (99.99%) by heating in air at 923 K for 24 h. o- TmMnO_3 was synthesized from hex- TmMnO_3 at 6 GPa and 1570 K for 2 h in an Au capsule. Single-phase hex- TmMnO_3 was synthesized from a stoichiometric mixture of Mn_2O_3 and Tm_2O_3 by annealing in air at ambient pressure at 1423 K for 80 h with several intermediate grindings. We note that the solubility limit of $(\text{Tm}_{1-x}\text{Mn}_x)\text{MnO}_3$ solid solutions was reported to be $x = 0.333$ [23]. However, we selected the $x = 0.3$ sample for neutron diffraction studies to be sure that the sample is single phase as small variations in real synthesis conditions could slightly shift the solubility limit.

X-ray powder diffraction (XRPD) data were collected at RT on a RIGAKU MiniFlex600 diffractometer using $\text{CuK}\alpha$ radiation (2θ range of 8° – 100° , a step width of 0.02° , and scan speed of $1^\circ/\text{min}$). Neutron powder diffraction experiments were performed on the high resolution powder diffractometer HRPT [26] at the Swiss Spallation Neutron Source (SINQ), Paul Scherrer Institut (PSI), Switzerland.

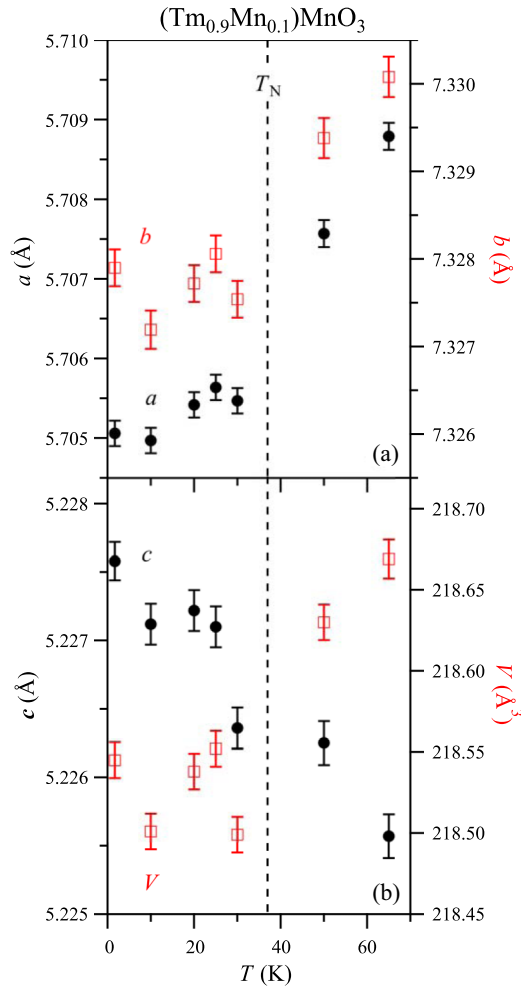


FIG. 2. Temperature dependence of the orthorhombic lattice parameters (a , b , and c) and the unit cell volume (V) in $(\text{Tm}_{0.9}\text{Mn}_{0.1})\text{MnO}_3$ refined from neutron diffraction data. The vertical dashed line indicates the Néel temperature $T_N = 37$ K.

Measurements at temperatures between 1.7 and 230 K and an incident neutron wavelength of 1.89 Å (2θ range of 3.55° – 164.50° , and a step width of 0.05°) were performed on $(\text{Tm}_{0.9}\text{Mn}_{0.1})\text{MnO}_3$ and $(\text{Tm}_{0.7}\text{Mn}_{0.3})\text{MnO}_3$ samples. The diffraction patterns were analyzed by the Rietveld method using the *FullProf Suite* [27]. Possible models for the magnetic structures were deduced based on a group theory analysis using the program *BasIreps* which is part of the *FullProf Suite* package of programs [27]. Strain broadening was modeled for (100) anisotropic broadening in an orthorhombic lattice using quartic form in reciprocal space [28,29]. Orthorhombic symmetry allows six independent strain parameters S_{HKL} [29]. Four of them (e.g., S_{040} , S_{004} , S_{220} , and S_{022}) turned out to be zero within experimental error, whereas the other two parameters, S_{400} and S_{202} , significantly deviated from zero and were refined.

Magnetic measurements were performed on a SQUID magnetometer (Quantum Design, MPMS-XL-7T) between 2 and 400 K in applied magnetic fields of 1 Oe, 100 Oe, and 10 kOe using both zero-field cooled (ZFC) and field cooled (FC) temperature scans. The inverse magnetic

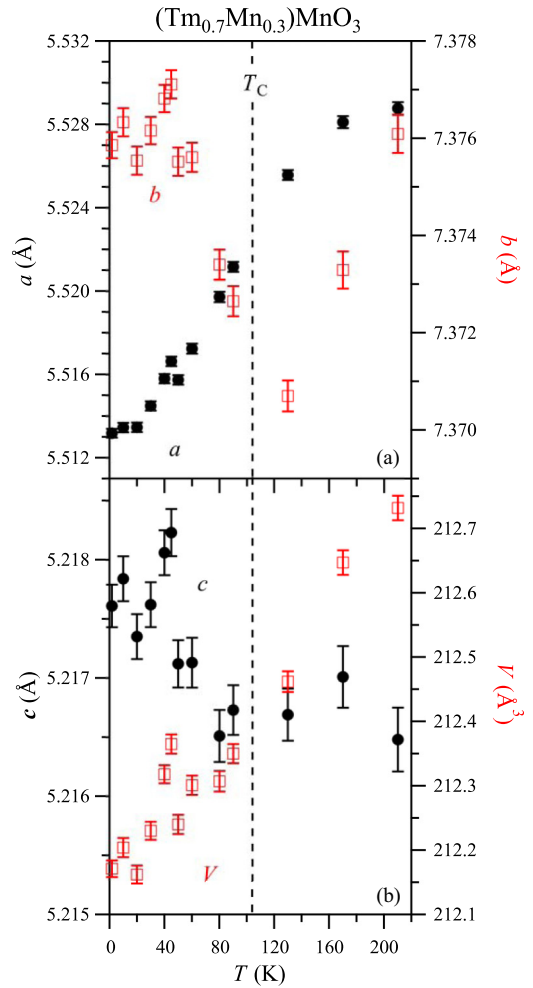


FIG. 3. Temperature dependence of the orthorhombic lattice parameters (a , b , and c) and the unit cell volume (V) in $(\text{Tm}_{0.7}\text{Mn}_{0.3})\text{MnO}_3$ refined from neutron diffraction data. The vertical dashed line indicates the ferrimagnetic ordering temperature $T_C = 104$ K.

susceptibility (χ^{-1}) was fitted using the Curie-Weiss equation

$$\chi(T) = \mu_{\text{eff}}^2 N [3k_B(T - \theta)]^{-1}, \quad (1)$$

where μ_{eff} is the effective magnetic moment, N is Avogadro's number, k_B is Boltzmann's constant, and θ is the Curie-Weiss temperature. For fitting we used the FCC curves measured at 10 kOe and temperature intervals between 250 and 395 K. Isothermal magnetization measurements were performed between -70 and 70 kOe at $T = 5$ K. Specific heat C_p at magnetic fields of 0 and 90 kOe (or 70 kOe) was recorded between 2 and 300 K on cooling and heating by a pulse relaxation method using a commercial calorimeter (Quantum Design PPMS). Dielectric properties were measured using a NOVOCONTROL Alpha-A High Performance Frequency Analyzer between 3 and 300 K on cooling and heating in the frequency range of 100 Hz and 2 MHz and in applied magnetic fields of 0 Oe and 90 kOe.

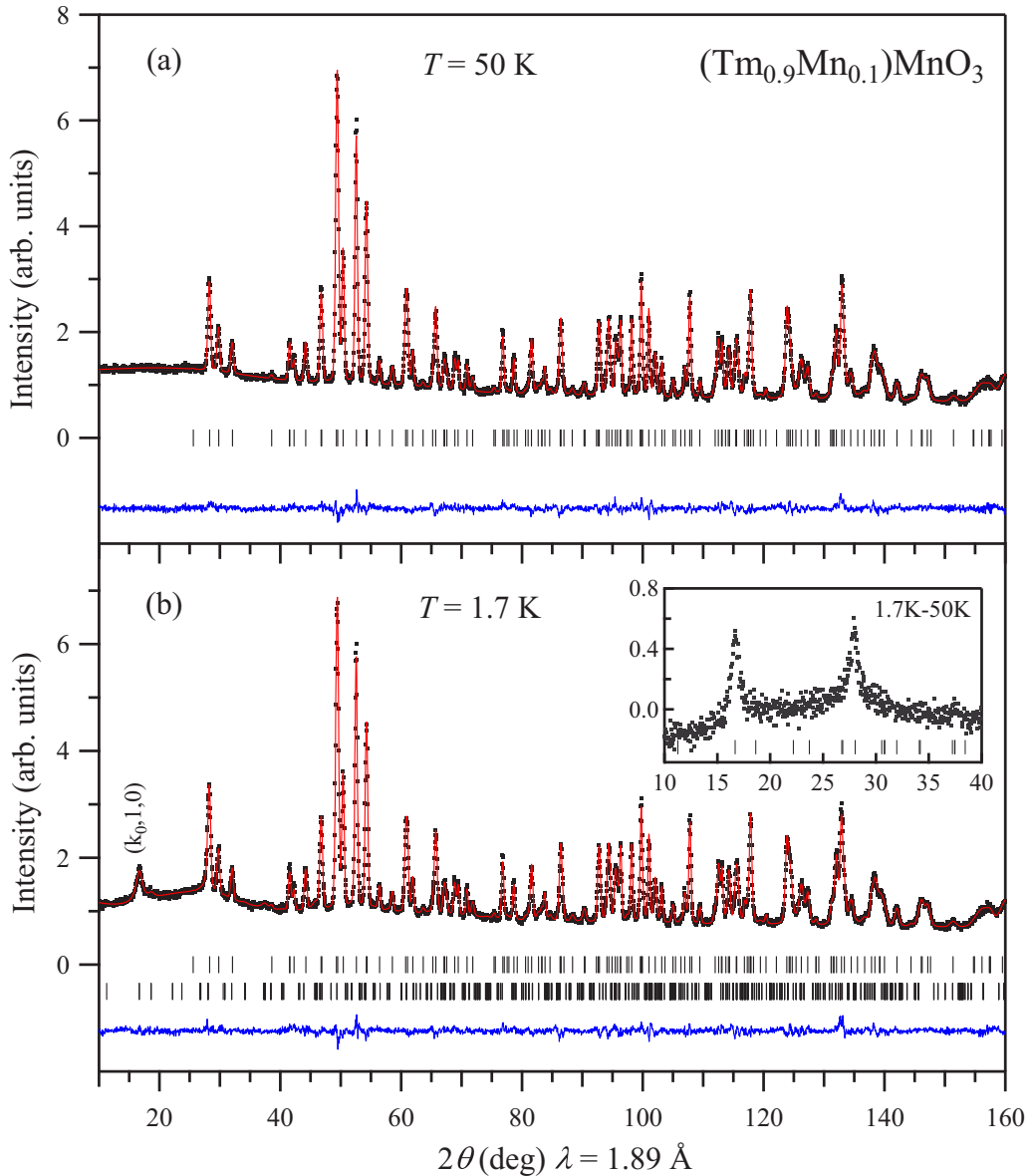


FIG. 4. Experimental (black dots), calculated (red line), and difference (blue line) neutron diffraction patterns of $(\text{Tm}_{0.9}\text{Mn}_{0.1})\text{MnO}_3$ (a) in the paramagnetic state at $T = 50$ K and (b) in the magnetically ordered state at $T = 1.7$ K. The tick marks indicate Bragg peak positions: the first row is for the nuclear peaks, and the second row is for the magnetic peaks. The inset shows part of the difference pattern 1.7–50 K with the two strongest magnetic Bragg peaks $(k_0, 1, 0)$ and $(1 - k_0, 1, 1)$ observed at the 2θ values 16.7° and 28.0° , respectively.

III. RESULTS AND DISCUSSION

A. Structural properties of $(\text{Tm}_{1-x}\text{Mn}_x)\text{MnO}_3$

Figure 1 gives the compositional dependence of the orthorhombic lattice parameters of $(\text{Tm}_{1-x}\text{Mn}_x)\text{MnO}_3$ ($0 \leq x \leq 0.333$) solid solutions. The a and c lattice parameters and the unit cell volume decrease monotonically with increasing x , while the b lattice parameter exhibits an increase. Changes from $x = 0$ to $x = 0.333$ are largest for a (decrease of $\Delta a \approx -0.30$ Å), followed by b (increase of $\Delta b \approx +0.07$ Å) and c (decrease of $\Delta c \approx -0.02$ Å). A similar compositional dependence has been observed in $(\text{Lu}_{1-x}\text{Mn}_x)\text{MnO}_3$ solid solutions between $x = 0$ and $x = 0.333$ with $\Delta a \approx -0.30$ Å, $\Delta b \approx +0.08$ Å, and $\Delta c \approx -0.02$ Å [24]. Figures 2 and 3 give the temperature dependence

of the orthorhombic lattice parameters (a , b , and c) and the unit cell volume (V) for $(\text{Tm}_{0.9}\text{Mn}_{0.1})\text{MnO}_3$ below $T = 65$ K and $(\text{Tm}_{0.7}\text{Mn}_{0.3})\text{MnO}_3$ below $T = 210$ K based on powder neutron diffraction data. For cooling $(\text{Tm}_{0.9}\text{Mn}_{0.1})\text{MnO}_3$ from $T = 65$ to 2 K, changes in the lattice parameters are rather small with a decrease for a ($\Delta a \approx -0.004$ Å) and b ($\Delta b \approx -0.003$ Å) and an increase for c ($\Delta c \approx +0.002$ Å). In $(\text{Tm}_{0.7}\text{Mn}_{0.3})\text{MnO}_3$ with a higher Mn self-doping, a pronounced minimum for the b lattice parameter appears near the ferrimagnetic ordering temperature T_C . A similar minimum for b near T_C has been observed in $(\text{Lu}_{0.6}\text{Mn}_{0.4})\text{MnO}_3$ [24]. For cooling $(\text{Tm}_{0.7}\text{Mn}_{0.3})\text{MnO}_3$ from $T_C = 104$ to 2 K, changes are largest for a (decrease of $\Delta a \approx -0.010$ Å), followed by b (increase of $\Delta b \approx +0.004$ Å) and c (small increase

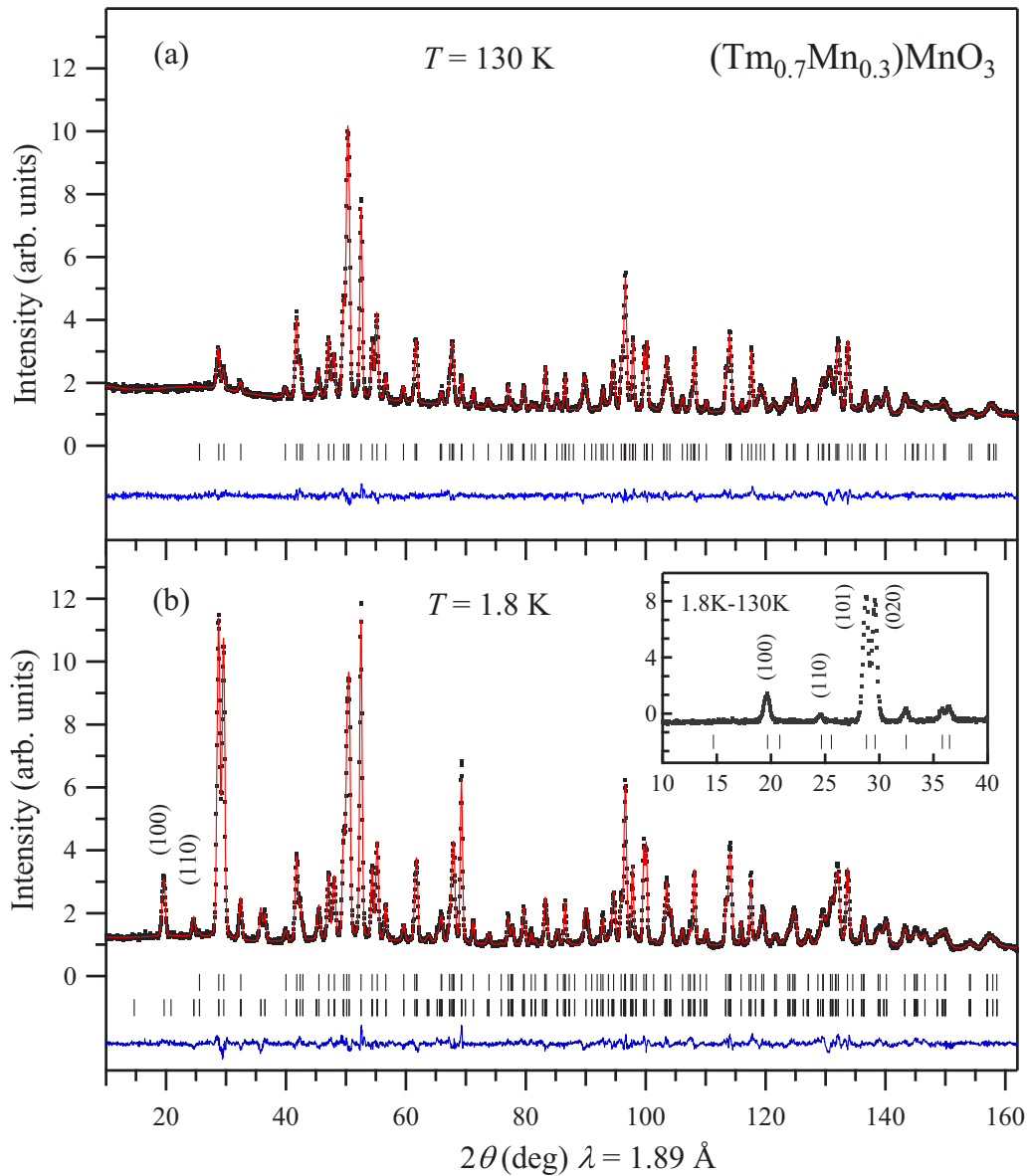


FIG. 5. Experimental (black dots), calculated (red line), and difference (blue line) neutron diffraction patterns of $(\text{Tm}_{0.7}\text{Mn}_{0.3})\text{MnO}_3$ (a) in the paramagnetic state at $T = 130$ K and (b) in the magnetically ordered state at $T = 1.8$ K. The tick marks indicate Bragg peak positions: the first row is for the nuclear peaks, and the second row is for the magnetic peaks. The inset shows part of the difference pattern 1.8–130 K.

of $\Delta c \approx +0.001$ Å). In comparison, for $(\text{Lu}_{0.6}\text{Mn}_{0.4})\text{MnO}_3$, changes between $T_C = 118$ and 2 K have been reported [24] to be $\Delta a \approx -0.004$ Å, $\Delta b \approx +0.004$ Å, and $\Delta c \approx -0.003$ Å. In particular, the temperature dependence of the a lattice parameter is much stronger in $(\text{Tm}_{0.7}\text{Mn}_{0.3})\text{MnO}_3$ compared to $(\text{Lu}_{0.6}\text{Mn}_{0.4})\text{MnO}_3$.

Experimental, calculated, and difference neutron diffraction patterns measured in the paramagnetic state are shown for $(\text{Tm}_{0.9}\text{Mn}_{0.1})\text{MnO}_3$ at $T = 50$ K in Fig. 4(a) and $(\text{Tm}_{0.7}\text{Mn}_{0.3})\text{MnO}_3$ at $T = 130$ K in Fig. 5(a). Rietveld refinements of the expected crystal structures give a poor agreement [$\chi^2 = 4.35$ for $(\text{Tm}_{0.9}\text{Mn}_{0.1})\text{MnO}_3$ and $\chi^2 = 7.18$ for $(\text{Tm}_{0.7}\text{Mn}_{0.3})\text{MnO}_3$] due to the presence of anisotropic line-shape broadening. Refinements that include corrections for strain broadening (details are described in Sec. II), give a much better agreement (χ^2 improved from 4.35

to 1.90 for $(\text{Tm}_{0.9}\text{Mn}_{0.1})\text{MnO}_3$ and from 7.18 to 2.10 for $(\text{Tm}_{0.7}\text{Mn}_{0.3})\text{MnO}_3$). Obtained structural parameters of o-TmMnO₃ (given for comparison), $(\text{Tm}_{0.9}\text{Mn}_{0.1})\text{MnO}_3$, and $(\text{Tm}_{0.7}\text{Mn}_{0.3})\text{MnO}_3$, strain parameters, bond lengths, Mn-O-Mn bond angles, and bond-valence sums (BVS) [30] are summarized in Tables I and II. The presence of Tm^{3+} and Mn^{2+} (with different sizes and masses) at the A site causes significant microstrain effects along the a direction which are absent in o-TmMnO₃ [7] and get stronger with increasing doping of Mn^{2+} . Compared to $(\text{Lu}_{1-x}\text{Mn}_x)\text{MnO}_3$ [24], larger values of the strain parameters indicate stronger strain effects in $(\text{Tm}_{1-x}\text{Mn}_x)\text{MnO}_3$. As a result of strain corrections, in the refinement of $(\text{Tm}_{1-x}\text{Mn}_x)\text{MnO}_3$, the values of the Debye-Waller factors B at the A and B sites tend to decrease from ~ 0.3 to ~ 0.1 Å². Probably due to correlations with the strain parameters, in the refinement of $(\text{Tm}_{0.9}\text{Mn}_{0.1})\text{MnO}_3$ at $T =$

TABLE I. Structure parameters of o-TmMnO₃ at $T = 50$ K [7], (Tm_{0.9}Mn_{0.1})MnO₃ at $T = 50$ K, and (Tm_{0.7}Mn_{0.3})MnO₃ at $T = 130$ K refined from powder neutron diffraction data.^a

| Site | WP | g | x | y | z | B (Å ²) |
|--|----|----------|------------|-----------|------------|-----------------------|
| o-TmMnO ₃ , $T = 50$ K | | | | | | |
| Tm | 4c | 1 | 0.0844(2) | 0.25 | 0.9826(3) | 0.42(3) |
| Mn2 | 4b | 1 | 0 | 0 | 0.5 | 0.51(5) |
| O1 | 4c | 1 | 0.4590(3) | 0.25 | 0.1174(3) | 0.43(3) |
| O2 | 8d | 1 | 0.3301(2) | 0.0550(1) | 0.6987(2) | 0.56(3) |
| (Tm _{0.9} Mn _{0.1})MnO ₃ , $T = 50$ K | | | | | | |
| Tm | 4c | 0.906(3) | 0.0826(2) | 0.25 | 0.9837(3) | 0.11(4) |
| Mn1 | 4c | 0.094(3) | = x (Tm) | 0.25 | = z (Tm) | = B (Tm) |
| Mn2 | 4b | 1 | 0 | 0 | 0.5 | 0.11 |
| O1 | 4c | 1 | 0.4600(3) | 0.25 | 0.11230(2) | 0.27(3) |
| O2 | 8d | 1 | 0.3244(2) | 0.0541(1) | 0.6975(2) | 0.35(3) |
| (Tm _{0.7} Mn _{0.3})MnO ₃ , $T = 130$ K | | | | | | |
| Tm | 4c | 0.698(3) | 0.0759(5) | 0.25 | 0.9826(4) | 0.08(7) |
| Mn1 | 4c | 0.302(3) | = x (Tm) | 0.25 | = z (Tm) | = B (Tm) |
| Mn2 | 4b | 1 | 0 | 0 | 0.5 | 0.36(5) |
| O1 | 4c | 1 | 0.4575(3) | 0.25 | 0.1076(3) | 0.64(4) |
| O2 | 8d | 1 | 0.3151(3) | 0.0539(2) | 0.6931(3) | 1.04(3) |

^aCrystal data: space group $Pnma$ (No. 62); $Z = 4$. WP = Wyckoff position. g is the occupation factor. The Mn2 notation is used in all compounds to mark Mn at the B sites for the uniformity.

$a = 5.8009(1)$ Å, $b = 7.3048(2)$ Å, $c = 5.2296(1)$ Å, and $V = 221.601(8)$ Å³;

$\chi^2 = 2.63$, $R_{wp} = 3.67\%$, $R_{exp} = 2.27\%$, and $R_{Bragg} = 2.84\%$;

for o-TmMnO₃ at $T = 50$ K.

$a = 5.7076(2)$ Å, $b = 7.3294(2)$ Å, $c = 5.2263(2)$ Å, and $V = 218.630(11)$ Å³;

strain parameters (in units of 10^{-4}): $S_{400} = 1.67(5)$, $S_{202} = 1.33(10)$;

$\chi^2 = 1.90$, $R_{wp} = 3.54\%$, $R_{exp} = 2.57\%$, and $R_{Bragg} = 3.70\%$;

for (Tm_{0.9}Mn_{0.1})MnO₃ at $T = 50$ K.

$a = 5.5256(2)$ Å, $b = 7.3707(3)$ Å, $c = 5.2167(2)$ Å, and $V = 212.462(16)$ Å³;

strain parameters (in units of 10^{-4}): $S_{400} = 4.22(9)$, $S_{202} = 1.75(21)$;

$\chi^2 = 2.10$, $R_{wp} = 3.79\%$, $R_{exp} = 2.62\%$, and $R_{Bragg} = 4.35\%$;

for (Tm_{0.7}Mn_{0.3})MnO₃ at $T = 130$ K.

TABLE II. Selected bond lengths (Å), bond angles (deg), bond valence sums (BVS), and distortion parameters of MnO₆ [Δ (Mn)] of o-TmMnO₃ at $T = 50$ K [7], (Tm_{0.9}Mn_{0.1})MnO₃ at $T = 50$ K, and (Tm_{0.7}Mn_{0.3})MnO₃ at $T = 130$ K.^a

| | o-TmMnO ₃ $T = 50$ K | (Tm _{0.9} Mn _{0.1})MnO ₃ $T = 50$ K | (Tm _{0.7} Mn _{0.3})MnO ₃ $T = 130$ K |
|-------------------------------|------------------------------------|--|---|
| Tm/Mn1 – O1 | 2.215(2) | 2.2209(19) | 2.207(3) |
| Tm/Mn1 – O1 | 2.284(2) | 2.258(2) | 2.236(3) |
| Tm/Mn1 – O2 ($\times 2$) | 2.2593(15) | 2.2648(15) | 2.237(2) |
| Tm/Mn1 – O2 ($\times 2$) | 2.5028(16) | 2.4905(16) | 2.473(2) |
| Tm/Mn1 – O2 ($\times 2$) | 2.5470(13) | 2.5494(13) | 2.5663(17) |
| BVS(Tm ³⁺) | 2.99 | 3.01 | 2.91 |
| BVS(Mn1 ²⁺) | – | 1.71 | 1.78 |
| Mn2 – O1 ($\times 2$) | 1.9413(5) | 1.9387(4) | 1.9405(5) |
| Mn2 – O2 ($\times 2$) | 1.9015(11) | 1.9135(11) | 1.9403(16) |
| Mn2 – O2 ($\times 2$) | 2.2154(11) | 2.1566(11) | 2.0504(16) |
| BVS(Mn2 ³⁺) | 3.17 | 3.24 | 3.37 |
| Δ (Mn2) | 47.7×10^{-4} | 29.7×10^{-4} | 6.88×10^{-4} |
| Mn2 – O1 – Mn2 ($\times 2$) | 140.35(2) | 141.875(17) | 143.45(2) |
| Mn2 – O2 – Mn2 ($\times 4$) | 142.97(4) | 143.80(4) | 144.37(7) |

^aBVS = $\sum_{i=1}^N \nu_i$, $\nu_i = \exp[(R_0 - l_i)/B]$, N is the coordination number, $B = 0.37$, $R_0(\text{Tm}^{3+}) = 2.000$, $R_0(\text{Mn}^{2+}) = 1.79$, and $R_0(\text{Mn}^{3+}) = 1.76$ [30].

$\Delta = (1/N) \sum_{i=1}^N [(l_i - l_{av})/l_{av}]^2$, where $l_{av} = (1/N) \sum_{i=1}^N l_i$ is the average Mn-O distance and N is the coordination number.

TABLE III. Magnetic arrangement allowed at the B site (4b) and A site (4c) for each of the irreducible representation (IR) based on group theory analysis (program *BasIRep* [27]) for space group $Pnma$ (No. 62 in International Tables for Crystallography [32]) and incommensurate magnetic propagation vector $\mathbf{k} = (k_0, 0, 0)$. $a^* = \exp(-i\pi k_0)$.

| Site 4b (B site) | | | | |
|---------------------------|--|------------------------------|--|--------------------------------|
| IR | Mn2 ₁ (0, 0, 1/2) | Mn2 ₂ (1/2, 0, 0) | Mn2 ₃ (0, 1/2, 1/2) | Mn2 ₄ (1/2, 1/2, 0) |
| Γ_1 | (u, v, w) | $a^* (-u, -v, w)$ | $(u, -v, w)$ | $a^* (-u, v, w)$ |
| Γ_2 | (u, v, w) | $a^* (u, v, -w)$ | $(-u, v, -w)$ | $a^* (-u, v, w)$ |
| Γ_3 | (u, v, w) | $a^* (-u, -v, w)$ | $(-u, v, -w)$ | $a^* (u, -v, -w)$ |
| Γ_4 | (u, v, w) | $a^* (u, v, -w)$ | $(u, -v, w)$ | $a^* (u, -v, -w)$ |
| Site 4c (A site), Orbit 1 | | | | |
| IR | Tm ₁ / Mn1 ₁ (0.08, 1/4, 0.98) | | Tm ₄ / Mn1 ₄ (0.58, 1/4, 0.52) | |
| Γ_1 | $(l_1, 0, n_1)$ | | $a^* (-l_1, 0, n_1)$ | |
| Γ_2 | $(0, m_1, 0)$ | | $a^*(0, m_1, 0)$ | |
| Γ_3 | $(0, m_1, 0)$ | | $a^*(0, -m_1, 0)$ | |
| Γ_4 | $(l_1, 0, n_1)$ | | $a^*(l_1, 0, -n_1)$ | |
| Site 4c (A site), Orbit 2 | | | | |
| IR | Tm ₂ / Mn1 ₂ (0.42, 3/4, 0.48) | | Tm ₃ / Mn1 ₃ (0.92, 3/4, 0.02) | |
| Γ_1 | $(l_2, 0, n_2)$ | | $a^* (-l_2, 0, n_2)$ | |
| Γ_2 | $(0, m_2, 0)$ | | $a^*(0, m_2, 0)$ | |
| Γ_3 | $(0, m_2, 0)$ | | $a^*(0, -m_2, 0)$ | |
| Γ_4 | $(l_2, 0, n_2)$ | | $a^*(l_2, 0, -n_2)$ | |

50 K, the value for B of Mn2 became unstable and has been fixed to 0.11 \AA^2 , the same value as obtained for B of Mn1 (see Table I). With the large contrast between the neutron scattering lengths $b_{\text{Tm}} = 7.07 \text{ fm}$ and $b_{\text{Mn}} = -3.73 \text{ fm}$, neutron data are sensitive to the occupation of Tm³⁺ and Mn²⁺ at the A site. The refinements gave values for Tm³⁺ [90.6(3)% for (Tm_{0.9}Mn_{0.1})MnO₃ and 69.8(3)% for (Tm_{0.7}Mn_{0.3})MnO₃] that are close to the nominal composition.

o-TmMnO₃ has a very large octahedral distortion parameter of $\Delta = 47.7 \times 10^{-4}$, which is comparable with that of o-HoMnO₃ ($\Delta = 48.9 \times 10^{-4}$) [6] and o-LuMnO₃ ($\Delta = 49.1 \times 10^{-4}$) [24], originating from a strong Jahn-Teller distortion. The octahedral distortion parameter reduces in (Tm_{1-x}Mn_x)MnO₃ with increasing x because of the increased amount of Mn⁴⁺ at the B site. The BVS values of the A sites were very close to the expected value of +3 for Tm³⁺, but were reduced to about +1.7 to +1.8 for Mn²⁺ because the size of Mn²⁺ is noticeably smaller than that of Tm³⁺. The BVS values of the B sites were slightly larger than +3 in o-TmMnO₃, but the same behavior was observed in other RMnO₃ perovskites (e.g., BVS = +3.14 in o-HoMnO₃ and +3.20 in o-LuMnO₃) [6,24]. The BVS values of the B sites increase in (Tm_{1-x}Mn_x)MnO₃ with increasing x because of the increased amount of Mn⁴⁺ at the B site.

B. Magnetic structures of (Tm_{1-x}Mn_x)MnO₃

1. Magnetic structure of (Tm_{0.9}Mn_{0.1})MnO₃

The neutron diffraction pattern of (Tm_{0.9}Mn_{0.1})MnO₃ at 1.7 K shown in Fig. 4(b) features new rather weak magnetic Bragg peaks due to long-range magnetic order and broad diffuse magnetic intensity due to short-range magnetic order. The two strongest magnetic Bragg peaks at $2\theta = 16.7^\circ$ and

28.0° are displayed with expanded scale in the difference pattern 1.7–50 K shown in the inset of Fig. 4(b). Long-range magnetic order at 1.7 K corresponds to an IC magnetic propagation vector $\mathbf{k} = (k_0, 0, 0)$ with $k_0 = 0.406(1)$. In order to investigate the magnetic structure that accords with the space group $Pnma$ and the IC propagation vector $\mathbf{k} = (k_0, 0, 0)$, we employed the group theory analysis calculated by the program *BasIRep* [27]. In Table III the irreducible representations (IR) for the magnetic structures allowed at the B site (4b) and A site (4c) are summarized. There are four IR (Γ_1 , Γ_2 , Γ_3 , and Γ_4) with different symmetry and the basis vectors are complex. All IR are one-dimensional:

$$\Gamma_{\text{Mn2(B site)}} = 3\Gamma_1 + 3\Gamma_2 + 3\Gamma_3 + 3\Gamma_4,$$

$$\Gamma_{\text{Orbit1,Tm/Mn1(A site)}} = 2\Gamma_1 + \Gamma_2 + \Gamma_3 + 2\Gamma_4,$$

$$\Gamma_{\text{Orbit2,Tm/Mn1(A site)}} = 2\Gamma_1 + \Gamma_2 + \Gamma_3 + 2\Gamma_4.$$

At the B site, all four Mn2 atoms located at $y = 0$ and $y = 1/2$ are coupled by symmetry. In Table III the direction of the magnetic Mn2 moments is described by the vectors (u, v, w) . At the A site, the four Tm/Mn1 atoms are split into two orbits without symmetry coupling. Orbit 1 contains the two Tm/Mn1 atoms located at $y = 1/4$ and the direction of the magnetic Tm/Mn1 moments is indicated by the vectors (l_1, m_1, n_1) . Orbit 2 contains the two Tm/Mn1 atoms located at $y = 3/4$ and the direction of the magnetic Tm/Mn1 moments is described by the vectors (l_2, m_2, n_2) .

To find the irreducible representation that describes the observed magnetic structure of (Tm_{0.9}Mn_{0.1})MnO₃ at 1.7 K, we have systematically fitted the scattering pattern to various possible magnetic structures. The best agreement has been obtained for a magnetic structure within IR Γ_2 , which allows an ordered magnetic moment along all three directions at the B site and only along the b axis at the A site. The

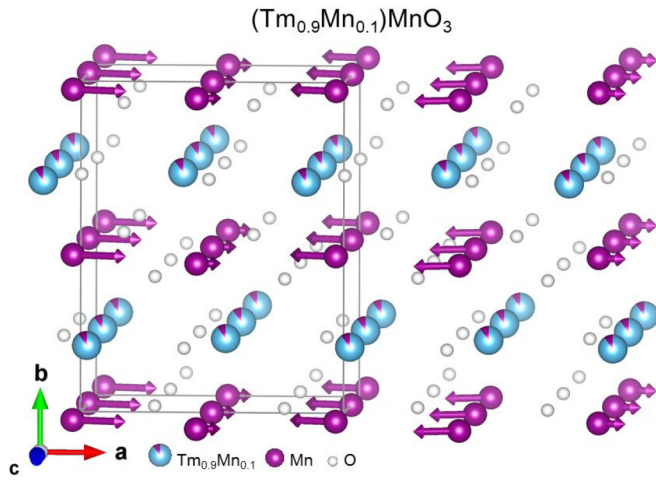


FIG. 6. Magnetic structure of $(\text{Tm}_{0.9}\text{Mn}_{0.1})\text{MnO}_3$ at 1.7 K (shown for $\varphi = 0$) determined by neutron diffraction. Ordered magnetic Mn moments are shown by arrows in purple. This drawing was made using the program VESTA [31].

refinement is shown in Fig. 4(b). Agreement values were $\chi^2 = 2.02$, $R_{\text{wp}} = 3.53\%$, $R_{\text{exp}} = 2.48\%$, $R_{\text{Bragg}} = 3.27\%$, and $R_{\text{Magnetic}} = 16.8\%$. The magnetic structure is plotted in Fig. 6. The 90% Mn^{3+} and 10% Mn^{4+} ions at the B site are ordered with an average amplitude given by $m_{\text{IC}} = \sqrt{2}(u, v, w) = \sqrt{2}[2.47(4), 0.0(3), 1.04(6)] \mu_B$, whereas the 90% Tm^{3+} and 10% Mn^{2+} ions at the A site were found to be disordered. Within experimental accuracy [$v = 0.0(3) \mu_B$], the ordered Mn moments at the B site lie inside the ac plane and the average amplitude varies between $\pm 3.79(6) \mu_B$. This value is very close to the maximum Mn moment of $3.9 \mu_B$ for 90% Mn^{3+} ($4.0 \mu_B$) and 10% Mn^{4+} ($3.0 \mu_B$) at the B site. Our neutron diffraction experiment can determine the amplitudes u (along a) and w (along c), but not the coupling between them which may be complex (phase φ). The observed neutron diffraction pattern agrees equally well for any value of the phase φ . In the general case, the magnetic structure at the B site is a *cycloid*, where both direction and size of the ordered Mn moments change. In the special cases ($\varphi = 0$ or $\varphi = \pi$), the magnetic structure at the B site is *amplitude modulated*, where the ordered Mn moments inside the ac plane form an angle of $\approx \pm 23^\circ$ with the a axis. The temperature dependence of the IC magnetic structure of $(\text{Tm}_{0.9}\text{Mn}_{0.1})\text{MnO}_3$ is shown in Fig. 7. The Mn ions at the B site order at $T_N = 37$ K and reach magnetic saturation at around $T = 10$ K. The magnetic propagation vector $\mathbf{k} = (k_0, 0, 0)$ shows a weak temperature dependence with k_0 increasing towards lower temperature and the magnetic structure has a small correlation length of only 12 nm that is almost constant below $T = 25$ K. Note that in the $(\text{Tm}_{1-x}\text{Mn}_x)\text{MnO}_3$ solid solutions, the correlation length of the commensurate magnetic structures at low temperature [~ 400 nm in o-TmMnO_3 and ~ 600 nm in $(\text{Tm}_{0.7}\text{Mn}_{0.3})\text{MnO}_3$] is an order of magnitude larger.

The accuracy of the determination of a possible long-range magnetic structure at the A site is limited by the low group theoretical symmetry with two orbits (see Table III) and by weak intensities of the observed magnetic Bragg peaks. For the A site, group theory analysis allows four additional

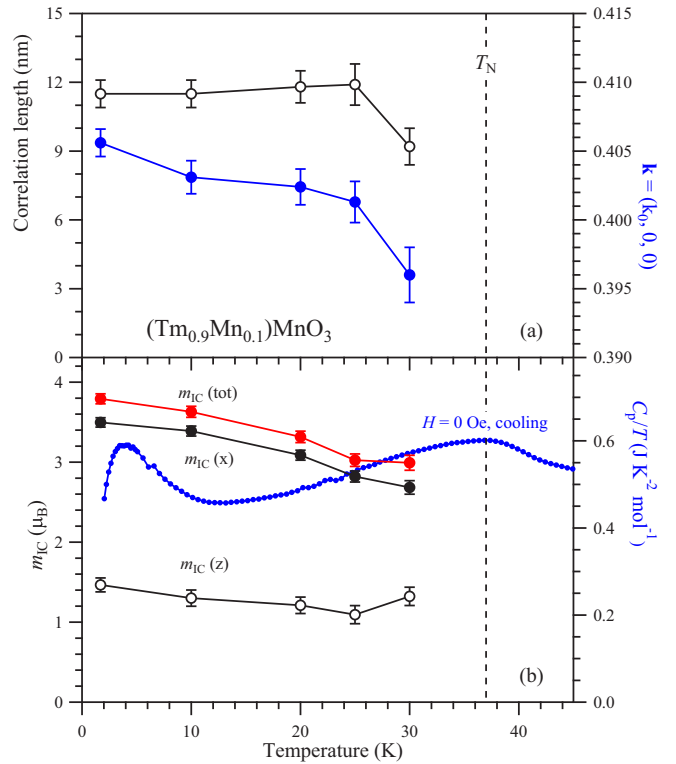


FIG. 7. Temperature dependence of the incommensurate magnetic structure of $(\text{Tm}_{0.9}\text{Mn}_{0.1})\text{MnO}_3$. Left-hand axes show the correlation length of the magnetic structure and the components of the ordered magnetic Mn moments m_{IC} at the B site; right-hand axes display the magnetic propagation vector and specific heat C_p/T . The vertical dashed line indicates the Néel temperature $T_N = 37$ K.

fitting parameters for the ordered moments (m_1 , m_2) and the phases (φ_1 , φ_2) which lead to different inequivalent neutron diffraction patterns. There are only two magnetic Bragg peaks with intensities that are clearly separated from the scattering of background data and one of them is covered by the much stronger $(1,0,1)$ Bragg peak of the crystal structure. Within experimental accuracy, the observed neutron diffraction pattern at 1.7 K can be well explained by ordering of magnetic Mn moments at the B site and there is no evidence for an additional ordered moment at the A site.

In addition to long-range magnetic order, also short-range magnetic order is observed in $(\text{Tm}_{0.9}\text{Mn}_{0.1})\text{MnO}_3$ at $T = 1.7$ K. The neutron diffraction pattern shown in Fig. 4(b) and with expanded scale in Fig. 8(a) features a broad peak of diffuse magnetic intensity (for $10^\circ < 2\theta < 40^\circ$) around the positions of the two strongest magnetic Bragg peaks $(k_0, 1, 0)$ and $(1 - k_0, 1, 1)$. In the following we compare the neutron diffraction patterns measured for $(\text{Tm}_{0.9}\text{Mn}_{0.1})\text{MnO}_3$ and $(\text{Tm}_{0.7}\text{Mn}_{0.3})\text{MnO}_3$ (Figs. 8 and 9). In the paramagnetic state the background contains an intensity contribution from disordered magnetic moments of Mn and Tm. This incoherent paramagnetic intensity is proportional to the square of the neutron magnetic form factor $F(\mathbf{Q})$ and decreases for increasing scattering vector \mathbf{Q} and for increasing 2θ values. In the magnetically ordered state, the incoherent paramagnetic intensity is replaced by coherent magnetic neutron scattering,

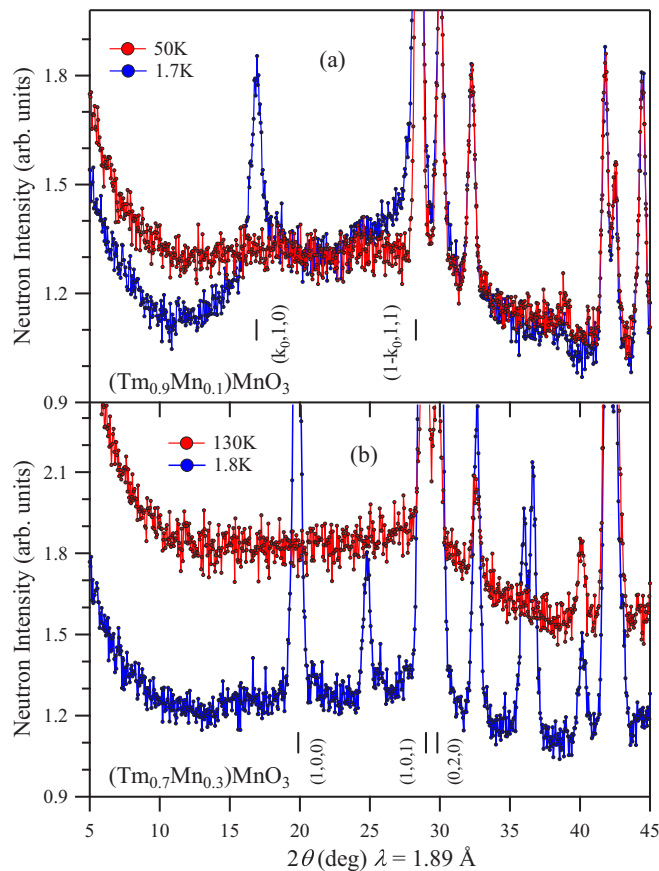


FIG. 8. Low angle part of neutron diffraction patterns measured in the paramagnetic and magnetically ordered states for (a) $(\text{Tm}_{0.9}\text{Mn}_{0.1})\text{MnO}_3$ and (b) $(\text{Tm}_{0.7}\text{Mn}_{0.3})\text{MnO}_3$, shown with an expanded scale. Tick marks indicate the position of Bragg peaks with the strongest magnetic intensity.

e.g., magnetic Bragg peaks for three-dimensional order. As shown in Fig. 8(b), such a behavior (smaller background and strong magnetic Bragg peaks at low temperature) has been nicely observed for $(\text{Tm}_{0.7}\text{Mn}_{0.3})\text{MnO}_3$ with a higher Mn self-doping and commensurate long-range ferrimagnetic order. The magnetic structure of $(\text{Tm}_{0.7}\text{Mn}_{0.3})\text{MnO}_3$ is presented in Sec. III B 2. The temperature dependence of neutron intensities observed at $2\theta = 10^\circ$ and $2\theta = 22.5^\circ$ plotted relative to the paramagnetic intensity of $(\text{Tm}_{0.7}\text{Mn}_{0.3})\text{MnO}_3$ at 130 K is displayed in Fig. 9(b). For both 2θ values, the neutron intensity decreases with a similar temperature dependence which is correlated to the release of magnetic entropy [C_p/T data also shown in Fig. 9(b)] and reach $\approx -35\%$ ($2\theta = 10^\circ$) and $\approx -30\%$ ($2\theta = 22.5^\circ$) at $T = 1.8$ K. The larger decrease for the smaller 2θ value reflects the larger value of the magnetic form factor $F(\mathbf{Q})$. For $(\text{Tm}_{0.9}\text{Mn}_{0.1})\text{MnO}_3$, Figure 9(a) shows the temperature dependence of neutron intensities measured at the same 2θ values and plotted relative to the paramagnetic intensity at $T = 50$ K. At $2\theta = 10^\circ$ (located outside the peak of diffuse magnetic intensity), the neutron intensity exhibits a decrease that is correlated to the release of magnetic entropy [C_p/T data also shown in Fig. 9(a)] and reaches $\approx -15\%$ at $T = 1.7$ K. However, at $2\theta = 22.5^\circ$ (located on top of the peak of diffuse magnetic intensity),

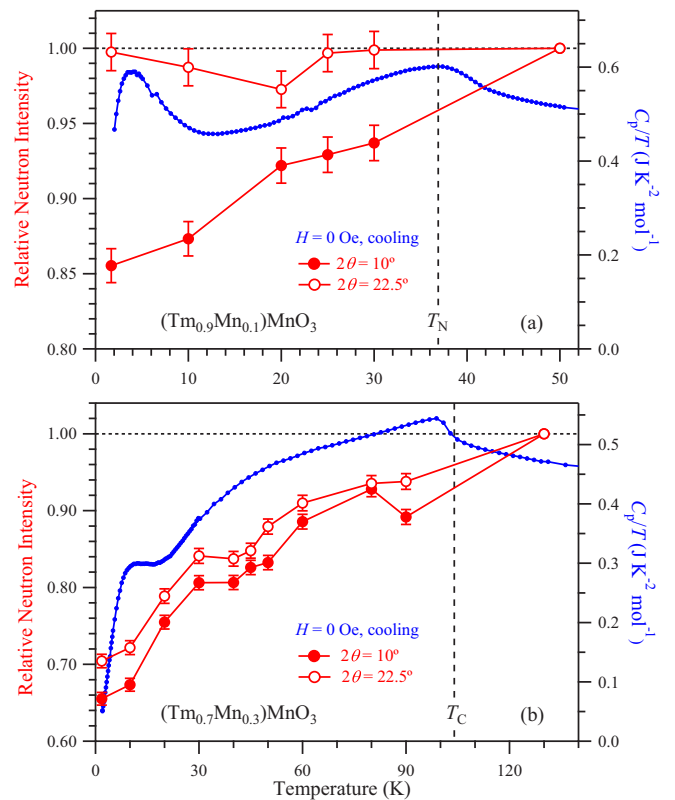


FIG. 9. Temperature dependence of neutron intensities observed at $2\theta = 10^\circ$ and $2\theta = 22.5^\circ$ (left-hand axes) and specific heat C_p/T (right-hand axes) measured for (a) $(\text{Tm}_{0.9}\text{Mn}_{0.1})\text{MnO}_3$ and (b) $(\text{Tm}_{0.7}\text{Mn}_{0.3})\text{MnO}_3$. Neutron intensities are shown as average of five data points (for $9.9^\circ \leq 2\theta \leq 10.1^\circ$ and $22.4^\circ \leq 2\theta \leq 22.6^\circ$) relative to the paramagnetic intensity at 50 K [$(\text{Tm}_{0.9}\text{Mn}_{0.1})\text{MnO}_3$] and 130 K [$(\text{Tm}_{0.7}\text{Mn}_{0.3})\text{MnO}_3$]. Vertical dashed lines indicate the antiferromagnetic ($T_N = 37$ K) and ferrimagnetic ($T_C = 104$ K) ordering temperatures.

the neutron intensity shows no decrease and remains almost unchanged down to the lowest measured temperature $T = 1.7$ K. The difference between the neutron intensities plotted in Fig. 9(a) demonstrates how short-range magnetic order in $(\text{Tm}_{0.9}\text{Mn}_{0.1})\text{MnO}_3$ appears around T_N , continues to increase towards an additional specific heat peak at $T = 4$ K, and remains at lower temperature. At the lowest measured temperature $T = 2$ K, the large value $C_p/T = 0.46$ J K $^{-2}$ mol $^{-1}$ indicates that part of the magnetic entropy is released at lower temperature. The absence of the broad peak of diffuse magnetic intensity in $(\text{Lu}_{0.9}\text{Mn}_{0.1})\text{MnO}_3$ [24] confirms that Tm^{3+} ions at the A site are involved in the short-range magnetic order observed in $(\text{Tm}_{0.9}\text{Mn}_{0.1})\text{MnO}_3$. Table IV compares the magnetic structure of $(\text{Tm}_{0.9}\text{Mn}_{0.1})\text{MnO}_3$ with that of $(\text{Lu}_{0.9}\text{Mn}_{0.1})\text{MnO}_3$. In both compounds, the B site is fully occupied by Mn^{3+} and Mn^{4+} ions. Magnetic ordering occurs at almost the same Néel temperature. The IC magnetic structures have the same symmetry Γ_2 and a comparably short correlation length. The presence of magnetic Tm^{3+} cations at the A site leads to a smaller k_0 component of the magnetic propagation vector and to a larger ordered Mn moment at the B site.

TABLE IV. Comparison of incommensurate magnetic structures of $(\text{Tm}_{0.9}\text{Mn}_{0.1})\text{MnO}_3$ and $(\text{Lu}_{0.9}\text{Mn}_{0.1})\text{MnO}_3$ at low temperature. Néel temperature T_N ; Magnetic propagation vector $\mathbf{k} = (k_0, 0, 0)$; irreducible representation (IR), and correlation length of magnetic structure.

| Compound Temperature (reference) | $(\text{Tm}_{0.9}\text{Mn}_{0.1})\text{MnO}_3$ $T = 1.7$ K (this work) | $(\text{Lu}_{0.9}\text{Mn}_{0.1})\text{MnO}_3$ $T = 2.0$ K [24] |
|--|---|--|
| T_N (K) | 37 | 36 |
| k_0 | 0.406(1) | 0.438(1) |
| IR | Γ_2 | Γ_2 |
| Correlation length | 12 nm | 20 nm |
| Ordered moment (B site): | | |
| Total: $ m_{\text{IC}} $ (μ_B) | 3.79(6) | 3.04(3) |
| x component: $m_{\text{IC},x}$ (μ_B) | 3.50(6) | 2.85(3) |
| y component: $m_{\text{IC},y}$ (μ_B) | 0.0(4) | 0.0(3) |
| z component: $m_{\text{IC},z}$ (μ_B) | 1.47(9) | 1.06(4) |
| Angle α (with a -axis) | $\approx 23^\circ$ | $\approx 20^\circ$ |
| Ordered moment (A site): | | |
| Total: $ m_{\text{IC}} $ (μ_B) | 0 | 0 |
| Short-range order | yes | no |

2. Magnetic structure of $(\text{Tm}_{0.7}\text{Mn}_{0.3})\text{MnO}_3$

The neutron diffraction pattern of $(\text{Tm}_{0.7}\text{Mn}_{0.3})\text{MnO}_3$ measured at 1.8 K contains strong magnetic Bragg peaks [Fig. 5(b)]. All magnetic reflections can be indexed with a commensurate propagation vector $\mathbf{k} = (0, 0, 0)$. Representation analysis was used to restrict the number of free parameters and to find the irreducible representation (IR) that describes the magnetic structure. A calculation by the program *BasIRep* [27] for $\mathbf{k} = (0, 0, 0)$ and space group *Pnma* gives the results summarized in Table V. There are eight IR with different symmetry. At the B site, all four Mn2 atoms are coupled by symmetry and four of the eight IR allow magnetic order. At the A site, all four Tm/Mn1 atoms are coupled by symmetry and decompose into eight different IR:

$$\begin{aligned}\Gamma_{\text{Mn2}}(\text{B site}) &= 3\Gamma_1 + 3\Gamma_3 + 3\Gamma_5 + 3\Gamma_7, \\ \Gamma_{\text{Tm/Mn1}}(\text{A site}) &= \Gamma_1 + 2\Gamma_2 + 2\Gamma_3 + \Gamma_4 \\ &\quad + \Gamma_5 + 2\Gamma_6 + 2\Gamma_7 + \Gamma_8.\end{aligned}$$

The observed magnetic structure of $(\text{Tm}_{0.7}\text{Mn}_{0.3})\text{MnO}_3$ at $T = 1.8$ K is ferrimagnetic and belongs to the IR Γ_7 , which allows ordered magnetic moments along all three directions (F_x, A_y, C_z) at the B site and within the ac -plane ($f_x, 0, c_z$) at the A site.

First we performed a refinement of the average ordered moments at A and B sites (Fit #1). The refinement at 1.8 K is shown in Fig. 5(b). Agreement values were $\chi^2 = 2.83$, $R_{\text{wp}} = 4.47$, $R_{\text{exp}} = 2.66$, $R_{\text{Bragg}} = 4.21$, and $R_{\text{Magnetic}} = 4.23$. The magnetic structure at 1.8 K based on Fit #1 is displayed in Fig. 10. At the B site, average ordered Mn moments are [$F_x = 3.15(3) \mu_B$, $A_y = 0.0(2) \mu_B$, $C_z = 0.0(3) \mu_B$]. Within experimental accuracy, they are ferromagnetically aligned along the a direction. The amplitude of $3.15(3) \mu_B$ is smaller than the maximum Mn moment of $3.7 \mu_B$ for 70% Mn^{3+} ($4.0 \mu_B$) and 30% Mn^{4+} ($3.0 \mu_B$). At the A site, the Tm^{3+} and Mn^{2+} ions are ordered with an average moment of [$f_x = -3.91(4) \mu_B$, $0, c_z = 2.35(2) \mu_B$]. The ordered moments of $4.56(4) \mu_B$ lie inside the ac plane and form an angle of $\approx \pm 31^\circ$ with the $-a$ direction. They are smaller than the maximum moment

TABLE V. Magnetic arrangement allowed at the B site and A site for each of the irreducible representation (IR) based on group theory analysis (program *BasIRep* [27]) for space group *Pnma* and commensurate magnetic propagation vector $\mathbf{k} = (0, 0, 0)$.

| IR | Site 4b (B site) Mn2 | Site 4c (A site) Tm/Mn1 | Magnetic space group [33] |
|-----------------------------|--|----------------------------|-------------------------------|
| Γ_1 | (G_x, C_y, A_z) | $(-, c_y, -)$ | <i>Pnma</i> (No. 62.1.502) |
| Γ_2 | | $(g_x, -, a_z)$ | <i>Pn'm'a'</i> (No. 62.9.510) |
| Γ_3 | (C_x, G_y, F_z) | $(c_x, -, f_z)$ | <i>Pn'm'a'</i> (No. 62.6.507) |
| Γ_4 | | $(-, g_y, -)$ | <i>Pnma'</i> (No. 62.5.506) |
| Γ_5 | (A_x, F_y, G_z) | $(-, f_y, -)$ | <i>Pn'm'a'</i> (No. 62.8.509) |
| Γ_6 | | $(a_x, -, g_z)$ | <i>Pnm'a'</i> (No. 62.4.505) |
| Γ_7 | (F_x, A_y, C_z) | $(f_x, -, c_z)$ | <i>Pnm'a'</i> (No. 62.7.508) |
| Γ_8 | | $(-, a_y, -)$ | <i>Pn'ma'</i> (No. 62.3.504) |
| $F = m_1 + m_2 + m_3 + m_4$ | | | $C = m_1 - m_2 + m_3 - m_4$ |
| $G = m_1 - m_2 - m_3 + m_4$ | | | $A = m_1 + m_2 - m_3 - m_4$ |
| B site | Mn2 ₁ (0, 0, 1/2), Mn2 ₂ (1/2, 0, 0), Mn2 ₃ (0, 1/2, 1/2), Mn2 ₄ (1/2, 1/2, 0) | | |
| A site | Tm/Mn1 ₁ ($x, 1/4, z$), Tm/Mn1 ₂ ($-x + 1/2, 3/4, z + 1/2$), Tm/Mn1 ₃ ($-x, 3/4, -z$), Tm/Mn1 ₄ ($x + 1/2, 1/4, -z + 1/2$) | | |

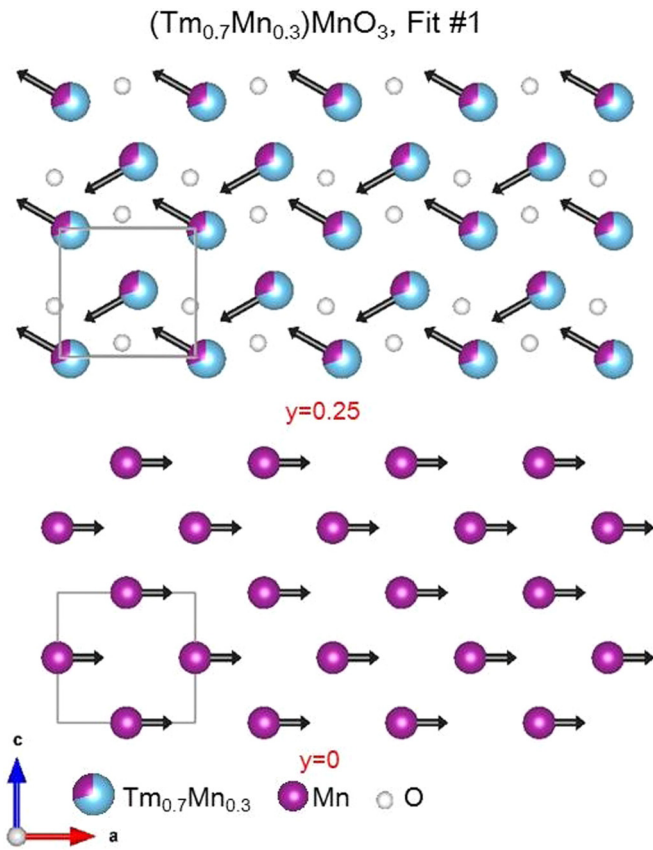


FIG. 10. Experimental 2D projections of the magnetic structures on the ac plane at $y = 0$ and $y = 0.25$ for (Tm_{0.7}Mn_{0.3})MnO₃ at 1.8 K based on Fit #1. Average ordered magnetic moments at the A and B sites are shown by black arrows. This drawing was made using the program VESTA [31].

of $6.4 \mu_B$ for 70% Tm³⁺ ($7.0 \mu_B$) and 30% Mn²⁺ ($5.0 \mu_B$). At 1.8 K, the magnetic structure contains a net macroscopic FM moment of $-0.76(6) \mu_B$ per formula unit. For a collinear ferrimagnetic structure with all ordered moments along the a direction, Bragg peaks of magnetic and crystal structures have the same extinction rules. The nonzero intensity observed for the purely magnetic (100) and (110) reflections [shown in the inset of Fig. 5(b)] is direct experimental evidence for the presence of a *noncollinear* ferrimagnetic structure in (Tm_{0.7}Mn_{0.3})MnO₃ at $T = 1.8$ K. Moreover, the nonzero intensity of the (110) Bragg peak implies the presence of a nonzero c_z component.

The temperature dependence of the magnetic structure of (Tm_{0.7}Mn_{0.3})MnO₃ based on Fit #1 is displayed in Fig. 11. The observed temperature dependence of the net macroscopic FM moment per formula unit determined by neutron diffraction and the FCC magnetic susceptibility measured in a very small magnetic field of $H = 1$ Oe are in good agreement [Fig. 11(a)]. The ferromagnetic moment ($F_x + f_x$) increases from 0 at $T_C = 104$ K to a maximum of $1.01(8) \mu_B$ at 60 K and then monotonically decreases towards $-0.76(6) \mu_B$ at 1.8 K by reaching negative values below 15.5 K. The temperature dependence of the three components (F_x , $-f_x$, c_z) of the average ordered magnetic moments is shown in Fig. 11(b). For the strongest purely magnetic (100) Bragg peak, neutron

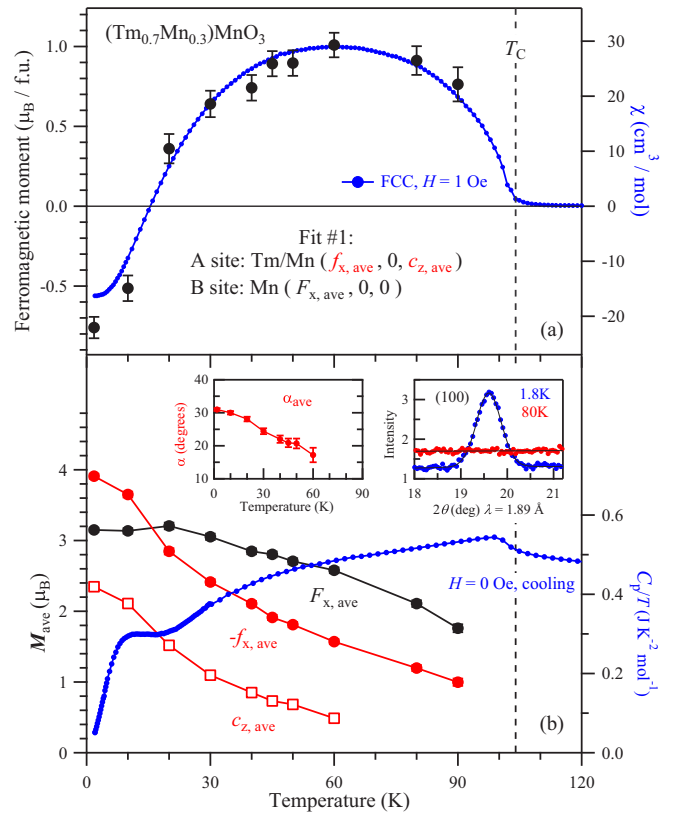


FIG. 11. Temperature dependence of the ferrimagnetic structure of (Tm_{0.7}Mn_{0.3})MnO₃ based on Fit #1. Left-hand axes show the macroscopic ferromagnetic moment per formula unit and the average ordered magnetic Tm and Mn moments at A and B sites; right-hand axes display the magnetic susceptibility χ (FCC, $H = 1$ Oe) and the specific heat C_p/T . The insets show the temperature dependence of the angle α_{ave} (between $-f_{x,ave}$ and $c_{z,ave}$) and the purely magnetic (100) reflection measured at 1.8 and 80 K. The vertical dashed line indicates the ferrimagnetic ordering temperature $T_C = 104$ K.

intensity has been detected up to 60 K, but not at higher temperatures [inset of Fig. 11(b)]. Therefore, the c_z component could be refined up to 60 K [Fig. 11(b)]. Below 60 K, the magnetic structure of (Tm_{0.7}Mn_{0.3})MnO₃ is *noncollinear*. Above 80 K, the magnetic structure is either *collinear* ($c_z = 0$) or *close to collinear* (with $c_z \neq 0$ being too small to be observed in our neutron diffraction measurements). With decreasing temperature, the ferromagnetically ordered Mn moments at the B site (F_x) monotonically increase below T_C and reach the saturation value at around 20 K. In contrast, the average ordered Tm and Mn moments at the A site ($-f_x$, c_z) exhibit an accelerated growth towards low temperature which is consistent with an additional anomaly observed in the specific heat [C_p/T data also shown in Fig. 11(b)].

We note that in the case of disordered Tm moments, the 30% of Mn²⁺ ions can produce a maximum average ordered moment of $1.5 \mu_B (= 0.3 \times 5.0 \mu_B)$ at the A site, which is too small to explain the experimentally observed ordered moments at all temperatures up to 60 K. This proves the presence of ordered Tm moments at temperatures up to at least 60 K. A (Tm_{1-x}Mn_x)MnO₃ sample with a slightly different composition $x = 0.333$ (very close to $x = 0.3$ of the present

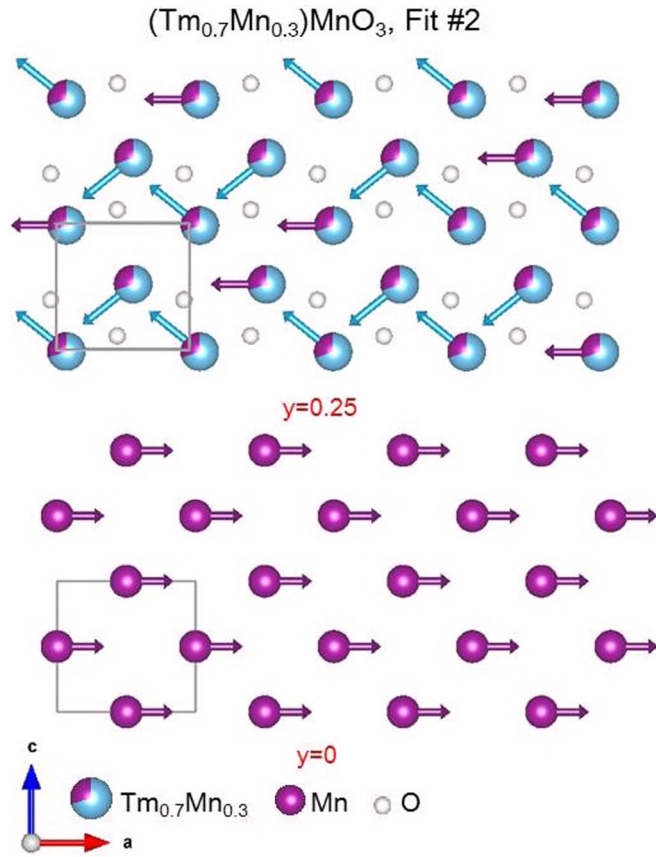


FIG. 12. Experimental 2D projections of the magnetic structures on the ac plane at $y = 0$ and $y = 0.25$ for (Tm_{0.7}Mn_{0.3})MnO₃ at 1.8 K based on Fit #2. Ordered magnetic moments are shown by arrows in purple (Mn) and blue (Tm). This drawing was made using the program VESTA [31].

study) has been studied in Ref. [23]. The difference between the specific heat C_p/T curves of (Tm_{0.667}Mn_{0.333})MnO₃ and (Lu_{0.667}Mn_{0.333})MnO₃ corresponds to the magnetic entropy from Tm which is released up to the Curie temperature $T_C = 106$ K of (Tm_{0.667}Mn_{0.333})MnO₃. Thus, an induced ordered magnetic Tm moment appears already at T_C .

In the refinement of average ordered moments at A and B sites (Fit #1), a strong temperature dependence has been observed for the direction of the average ordered moments at the A site as described by the increase of the angle α (between $-f_x$ and c_z) from $17.2^\circ (\pm 2.2^\circ)$ at 60 K to $31.0^\circ (\pm 0.4^\circ)$ at 1.8 K [inset of Fig. 11(b)]. Such a behavior may be caused by a superposition of Tm and Mn moments with different (temperature independent) directions that grow at different temperatures. We have searched for such a magnetic structure that is compatible with the observed neutron diffraction data. By systematically fixing and releasing fitting parameters, we have optimized and defined conditions and constraints for a second refinement (Fit #2) as follows:

$$\begin{aligned} \text{A site : Tm } & (f_{x,\text{Tm}}, 0, c_{z,\text{Tm}}); & c_{z,\text{Tm}} & = -0.85f_{x,\text{Tm}}, \\ \text{A site : Mn } & (f_{x,\text{Mn}}, 0, 0); & -f_{x,\text{Mn}} & = 1.23F_{x,\text{Mn}}, \\ \text{B site : Mn } & (F_{x,\text{Mn}}, 0, 0). \end{aligned}$$

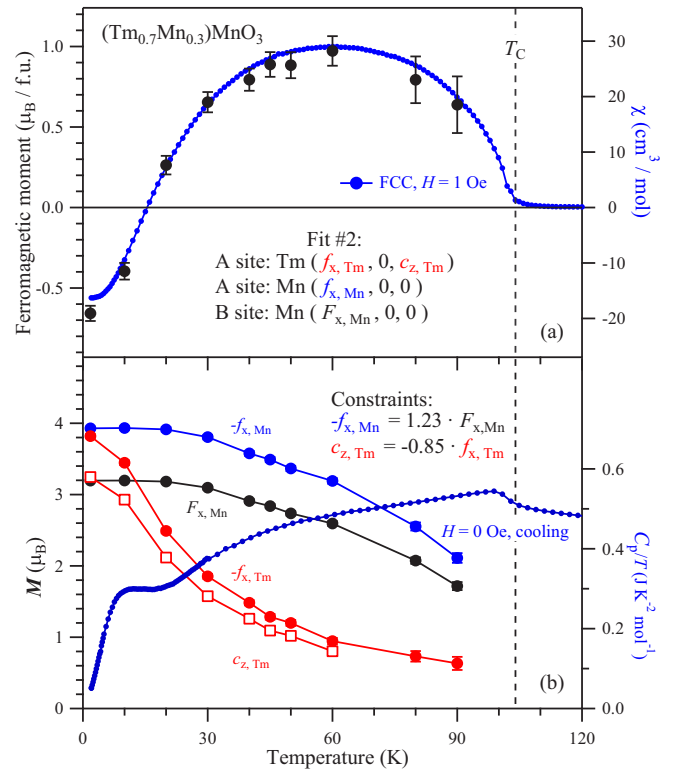


FIG. 13. Temperature dependence of the ferrimagnetic structure of (Tm_{0.7}Mn_{0.3})MnO₃ based on Fit #2. Left-hand axes show the macroscopic ferromagnetic moment per formula unit and the ordered magnetic Tm and Mn moments at A and B sites; right-hand axes display the magnetic susceptibility χ (FCC, $H = 1$ Oe) and the specific heat C_p/T . The vertical dashed line indicates the ferrimagnetic ordering temperature $T_C = 104$ K.

Taking into account the ferrimagnetic structure reported for (Lu_{0.6}Mn_{0.4})MnO₃ [24], we have fixed the direction of the ordered Mn moments at the A site to the $-a$ direction ($f_{x,\text{Mn}} \neq 0$, $c_{z,\text{Mn}} = 0$). The amplitude of the ordered Mn moments in (Lu_{0.6}Mn_{0.4})MnO₃ has been found to be larger at the A site ($-f_{x,\text{Mn}}$) than at the B site ($F_{x,\text{Mn}}$) [24]. To enforce this, we have correlated the two fitting parameters ($-f_{x,\text{Mn}}$, $F_{x,\text{Mn}}$) with a scale factor (1.23). Finally, we have fixed the direction of the ordered Tm moments to $\alpha_{\text{Tm}} = 40.4^\circ$, close to the Tm-Tm nearest neighbor direction ($\alpha = 47.1^\circ$).

The magnetic structure of (Tm_{0.7}Mn_{0.3})MnO₃ at 1.8 K based on Fit #2 is displayed in Fig. 12. Agreements values of the refinement were $\chi^2 = 2.81$, $R_{\text{wp}} = 4.45$, $R_{\text{exp}} = 2.66$, $R_{\text{Bragg}} = 4.11$, and $R_{\text{Magnetic}} = 4.12$. At 1.8 K, ordered magnetic moments at the A site are [$f_{x,\text{Tm}} = -3.82(3) \mu_B$, 0, $c_{z,\text{Tm}} = 3.25(3) \mu_B$] for Tm and [$f_{x,\text{Mn}} = -3.93(2) \mu_B$, 0, 0] for Mn. At the B site, Mn orders with [$F_{x,\text{Mn}} = -3.20(2) \mu_B$, 0, 0] and the macroscopic FM moment at 1.8 K was determined to be $-0.66(5) \mu_B$ per formula unit. The temperature dependence of the magnetic structure of (Tm_{0.7}Mn_{0.3})MnO₃ based on Fit #2 is shown in Fig. 13. The $c_{z,\text{Tm}}$ component has been refined up to 60 K.

Fit #1 (average ordered moments for Tm and Mn at the A site) and Fit #2 (different ordered moments for Tm and Mn at the A site) both explain the observed neutron diffraction

data quite well and support the following magnetic ordering process in $(\text{Tm}_{0.7}\text{Mn}_{0.3})\text{MnO}_3$. Mn-Mn exchange interactions ($3d$ electron magnetism) are stronger than (Tm-Tm) exchange interactions ($4f$ electron magnetism) and Tm-Mn exchange interactions. In $(\text{Tm}_{0.7}\text{Mn}_{0.3})\text{MnO}_3$, the Mn moments at the A and B sites order at $T_C = 104$ K with a ferrimagnetic structure similar to that observed in $(\text{Lu}_{0.6}\text{Mn}_{0.4})\text{MnO}_3$ and reach magnetic saturation at around 20 K. The ordering of magnetic Mn moments at $T_C = 104$ K triggers magnetic ordering of the Tm^{3+} cations also at T_C with a small ordered Tm moment parallel (or almost parallel) to that of Mn^{2+} at the A site. Below $T = 60$ K, the maximum of the macroscopic ferromagnetic moment, the Tm moments adopt the zigzag magnetic structure shown in Fig. 12, which contains a macroscopic ferromagnetic moment that aligns with the direction of the ordered Mn^{2+} moments. Towards low temperature, the Tm-Tm exchange interactions produce a strong increase of the ordered Tm moments from $1.24(6) \mu_B$ at 60 K to $5.02(4) \mu_B$ at 1.8 K. The macroscopic FM moment of 100% of Mn^{3+} and Mn^{4+} ions at the B site is reduced by the FM moment of 30% of Mn^{2+} ions at the A site. But the additional FM component of the magnetic structure of 70% of Tm^{3+} ions at the A site is necessary to overcompensate it and realize the negative magnetization effect in $(\text{Tm}_{0.7}\text{Mn}_{0.3})\text{MnO}_3$ with a compensation temperature of 15.5 K.

C. Magnetic and dielectric properties of $(\text{Tm}_{1-x}\text{Mn}_x)\text{MnO}_3$

Figures 14 and 15 show the ZFC and FCC χ vs T magnetic susceptibilities of $(\text{Tm}_{1-x}\text{Mn}_x)\text{MnO}_3$, $0 \leq x \leq 0.3$, measured under magnetic fields of 100 Oe and 10 kOe. For o- TmMnO_3 , no difference was observed between the ZFC and FCC curves and no clear magnetic anomalies were detected at T_{N1} and T_{N2} in agreement with previous reports [7,34]. o- TmMnO_3 exhibits basically paramagneticlike behavior that originates from the dominant contribution of Tm^{3+} . The magnetic transition temperatures T_{N1} and T_{N2} could only be seen by very small bumps in the differential curves $d\chi T/dT$ vs T , shown in the inset of Fig. 14. $(\text{Tm}_{0.9}\text{Mn}_{0.1})\text{MnO}_3$ showed more pronounced anomalies at the magnetic ordering temperature $T_N = 37$ K. Under the smaller magnetic field, $H = 100$ Oe, clear peaks were observed at T_N with a divergence between the ZFC and FCC curves, while under the stronger magnetic field, $H = 10$ kOe, a kink at T_N was measured without noticeable difference between the ZFC and FCC curves. At low temperatures, the χ vs T curves continue to rise with decreasing temperature due to a paramagnetic contribution from Tm^{3+} . The χ vs T curves of $(\text{Tm}_{0.8}\text{Mn}_{0.2})\text{MnO}_3$ and $(\text{Tm}_{0.7}\text{Mn}_{0.3})\text{MnO}_3$ were principally different from those of o- TmMnO_3 and $(\text{Tm}_{0.9}\text{Mn}_{0.1})\text{MnO}_3$ [35]. The ZFC curves started from small values and demonstrated broad maxima when approaching T_C . We determined T_C from sharp peaks on the 100 Oe FCC $d\chi T/dT$ vs T curves. The FCC curves increased sharply below T_C , passed through maxima, and finally reduced to negative values. In other words, the FCC curves demonstrated magnetization reversal or negative magnetization effects. The compensation temperature (where the magnetization takes the zero value) is almost the same in the two compounds ($T_{\text{comp}} = 14.5\text{--}15$ K at $H = 100$ Oe). At high temperature, the inverse magnetic susceptibilities follow

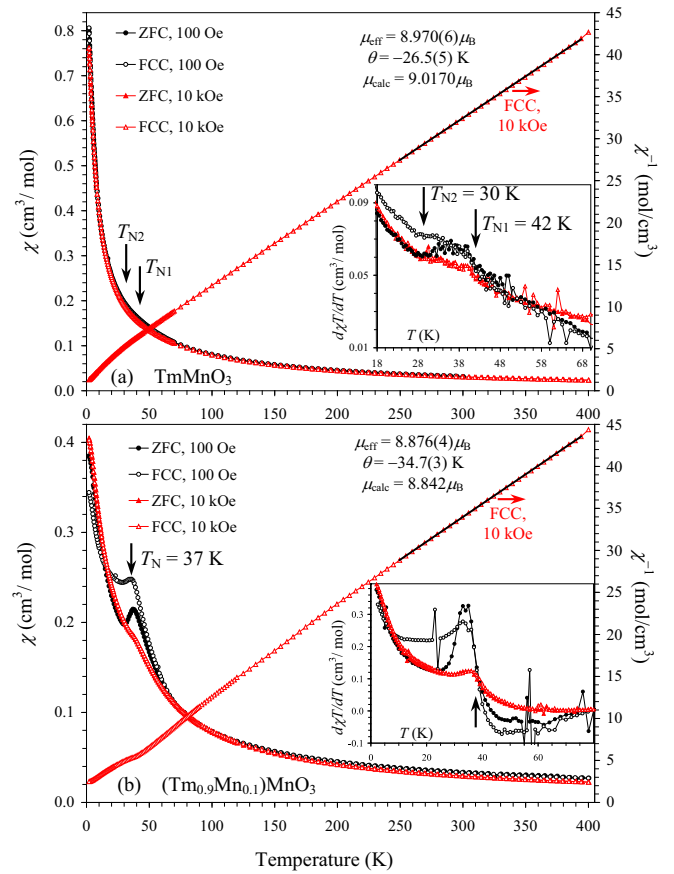


FIG. 14. ZFC (filled symbols) and FCC (empty symbols) DC magnetic susceptibility ($\chi = M/H$) curves of (a) o- TmMnO_3 and (b) $(\text{Tm}_{0.9}\text{Mn}_{0.1})\text{MnO}_3$. Left-hand axes give the χ vs T curves at 100 Oe (black) and 10 kOe (red); right-hand axes give the 10 kOe FCC χ^{-1} vs T curves with the Curie-Weiss fits and fitting parameters. (Insets) $d\chi T/dT$ vs T curves to highlight magnetic anomalies.

the Curie-Weiss law with the parameters given in Figs. 14 and 15 [for the calculated effective magnetic moments we used $\mu(\text{Tm}^{3+}) = 7.57 \mu_B$].

As we found from our magnetic structure determinations, the origin of negative magnetization in $(\text{Tm}_{0.7}\text{Mn}_{0.3})\text{MnO}_3$ lies in its ferrimagnetic structure and different temperature dependence of the sublattice magnetizations. At T_C , all magnetic cations probably exhibit long-range ordering ($T_{N,\text{Tm}} = T_{N,\text{Mn}}$). But the total magnetic moment at the B site is much larger in the vicinity of T_C because Tm^{3+} has a small moment and the concentration of the $3d$ transition metal at the A site is small. Therefore, a preferential domain structure is built where the magnetic moments at the B site lie in the direction of a magnetic field, and the magnetic moments at the A site lie in the opposite direction. With decreasing temperature, the magnetic moments of all manganese cations saturate and reach nearly the constant values, while the total magnetic moment at the A site continues to rise due to the increase of the Tm^{3+} moment. At the compensation point, the total magnetic moment of the A site overcomes the total magnetic moment at the B site. At small measurement magnetic fields below a coercive field at a certain temperature, the total moment now lies in the opposite direction compared with an

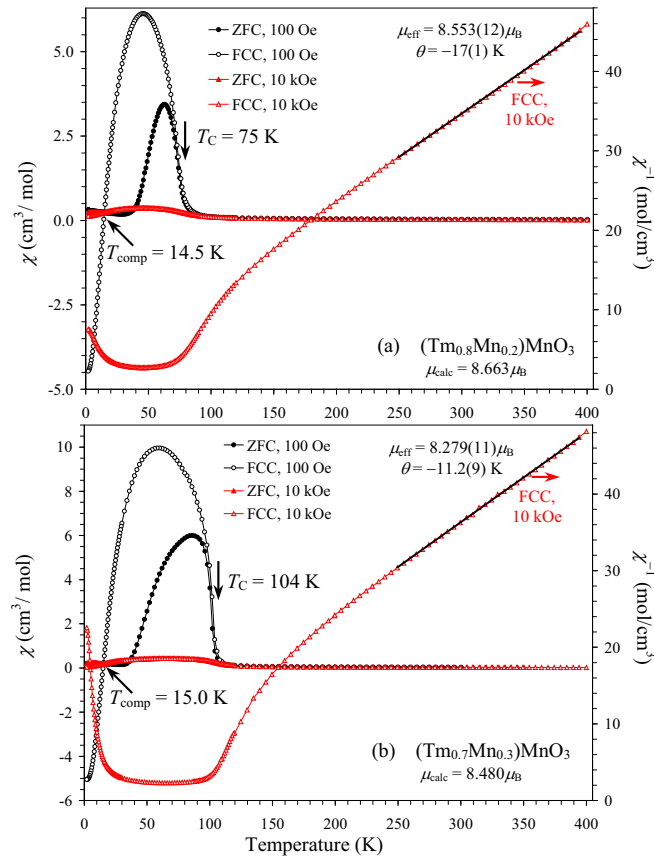


FIG. 15. ZFC (filled symbols) and FCC (empty symbols) DC magnetic susceptibility ($\chi = M/H$) curves of (a) $(\text{Tm}_{0.8}\text{Mn}_{0.2})\text{MnO}_3$ and (b) $(\text{Tm}_{0.7}\text{Mn}_{0.3})\text{MnO}_3$. Left-hand axes give the χ vs T curves at 100 Oe (black) and 10 kOe (red); right-hand axes give the 10 kOe FCC χ^{-1} vs T curves with the Curie-Weiss fits and fitting parameters. T_{comp} is the compensation temperature, where the magnetization takes the zero value.

applied field resulting in the observed negative magnetization. Large magnetic fields can change magnetization in each domain resulting in the disappearance of negative magnetization. This is a classical mechanism of the magnetization reversal effect proposed by Néel [36]. The similar magnetic properties of $(\text{Tm}_{0.8}\text{Mn}_{0.2})\text{MnO}_3$, $(\text{Tm}_{0.7}\text{Mn}_{0.3})\text{MnO}_3$, and $(\text{Tm}_{0.667}\text{Mn}_{0.333})\text{MnO}_3$ suggest that they have similar ferrimagnetic structures. This fact means that the presence of only 20% of $3d$ transition metals at the A site (this value is below the percolation threshold of 31%) can drastically modify the behavior of magnetic rare-earth cations at the A site in simple GdFeO_3 -type perovskites. We remind that Tm^{3+} cations are ordered only below $T_{N3,\text{Tm}} = 4$ K in undoped o- TmMnO_3 [7].

Figure 16 shows isothermal magnetization curves (M vs H) at $T = 5$ K. No hysteresis was observed in o- TmMnO_3 and $(\text{Tm}_{0.9}\text{Mn}_{0.1})\text{MnO}_3$ in agreement with their IC and antiferromagnetic structures with a zero net magnetization. They just have an S-type shape originating from paramagnetic Tm^{3+} contributions. The M vs H curves for the $x = 0.2, 0.3$, and 0.333 samples were very similar to each other reflecting the same magnetic structure. They showed well-defined, extended hysteresis originating from the ferrimagnetic

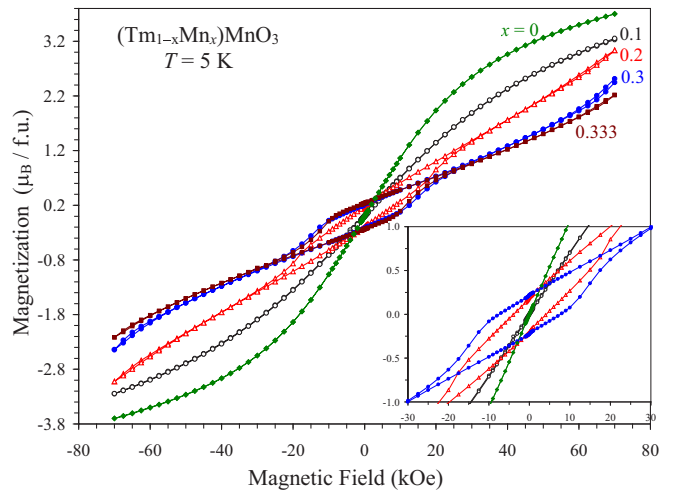


FIG. 16. M vs H curves at $T = 5$ K for $(\text{Tm}_{1-x}\text{Mn}_x)\text{MnO}_3$ solid solutions with $x = 0, 0.1, 0.2, 0.3$, and 0.333 [22]. f.u.: formula unit. (Inset) Details near the origin.

structures. In addition, $(\text{Tm}_{0.7}\text{Mn}_{0.3})\text{MnO}_3$ clearly showed an upturn of magnetization above about 60 kOe suggesting the existence of a field-induced transition. Field-induced transitions near 11 K were also detected on the χ vs T curves of $(\text{Tm}_{0.7}\text{Mn}_{0.3})\text{MnO}_3$ when measured above 15 kOe.

Specific heat data of $(\text{Tm}_{1-x}\text{Mn}_x)\text{MnO}_3$, $0 \leq x \leq 0.3$, plotted as C_p/T vs T , are presented in Fig. 17. For o- TmMnO_3 , two specific heat anomalies at T_{N1} and T_{N2} were observed for heating with a hysteresis indicating a first-order phase transition at T_{N2} . On the other hand, $(\text{Tm}_{0.9}\text{Mn}_{0.1})\text{MnO}_3$ showed just one quite broad anomaly at T_N without any hysteresis for cooling and heating. An additional peak at $T = 4$ K originates from the release of magnetic entropy from Tm^{3+} . $(\text{Tm}_{0.8}\text{Mn}_{0.2})\text{MnO}_3$ had a quite weak anomaly at T_C , but it showed an additional sharper anomaly at $T = 7.5$ K due to an enhanced entropy release from Tm^{3+} . Compared to $(\text{Tm}_{0.8}\text{Mn}_{0.2})\text{MnO}_3$, $(\text{Tm}_{0.7}\text{Mn}_{0.3})\text{MnO}_3$ showed a more well-defined anomaly at T_C and a broader additional anomaly at $T = 7.5$ K. In both compounds, magnetic fields made the low-temperature anomalies sharper. In addition, a hysteresis observed near $T = 7.5$ K under $H = 90$ K Oe indicated a first-order field-induced magnetic phase transition in $(\text{Tm}_{0.7}\text{Mn}_{0.3})\text{MnO}_3$.

Figure 18 shows the temperature dependence of dielectric constant in $(\text{Tm}_{0.9}\text{Mn}_{0.1})\text{MnO}_3$ and $(\text{Tm}_{0.8}\text{Mn}_{0.2})\text{MnO}_3$ measured under $H = 0$ Oe and 90 kOe for cooling and heating. No temperature hysteresis was observed and no significant difference between the curves measured at 0 Oe and 90 kOe. The latter observation suggests that the magnetodielectric effect is negligible. Dielectric properties of $(\text{Tm}_{0.9}\text{Mn}_{0.1})\text{MnO}_3$ and $(\text{Tm}_{0.8}\text{Mn}_{0.2})\text{MnO}_3$ were very similar with those of $(\text{Lu}_{0.9}\text{Mn}_{0.1})\text{MnO}_3$ and $(\text{Lu}_{0.8}\text{Mn}_{0.2})\text{MnO}_3$ [24]. With decreasing temperature, the dielectric constant of $(\text{Tm}_{0.9}\text{Mn}_{0.1})\text{MnO}_3$ starts to gradually increase when approaching T_N . Then, without any clear anomaly at T_N , it passes through a very broad maximum near $T = 13$ K. $(\text{Tm}_{0.8}\text{Mn}_{0.2})\text{MnO}_3$ shows no dielectric anomalies at and near T_C .

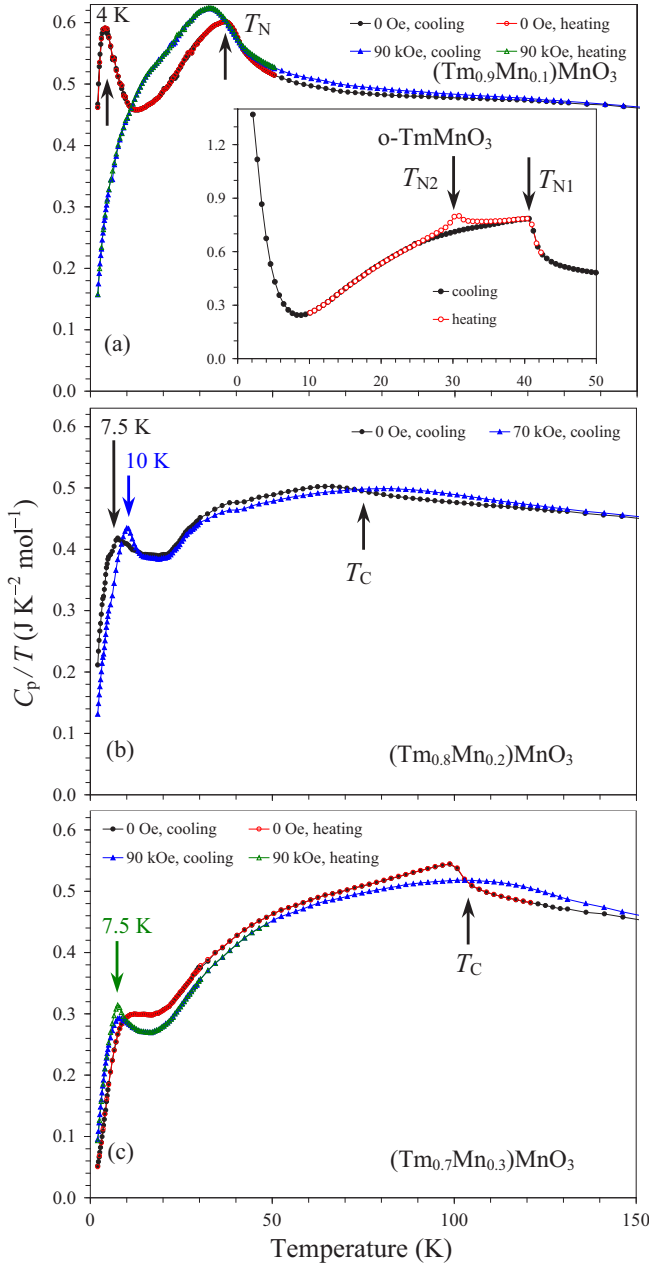


FIG. 17. Specific heat data of (a) $(\text{Tm}_{0.9}\text{Mn}_{0.1})\text{MnO}_3$, (b) $(\text{Tm}_{0.8}\text{Mn}_{0.2})\text{MnO}_3$, and (c) $(\text{Tm}_{0.7}\text{Mn}_{0.3})\text{MnO}_3$ plotted as C_p/T vs T at different magnetic fields. (Inset) The C_p/T vs T curves of o-TmMnO_3 at $H = 0$ Oe on cooling and heating [4].

IV. CONCLUSION

By means of magnetic, dielectric, and neutron diffraction measurements we have investigated how the physical properties and magnetic structures evolve in $(\text{Tm}_{1-x}\text{Mn}_x)\text{MnO}_3$ solid solutions with $0 \leq x \leq 0.3$. We found that the introduction of magnetic Mn^{2+} cations into the A site leads to an incommensurate spin structure for $x = 0.1$ and to a ferrimagnetic structure with magnetization reversal for $x \geq 0.2$. Commensurate magnetic structures have a much larger correlation length (~ 400 nm for $x = 0$, ~ 600 nm for $x = 0.3$) than the incommensurate magnetic structure (~ 12 nm for $x = 0.1$). The presence of Tm^{3+} and Mn^{2+} (with different

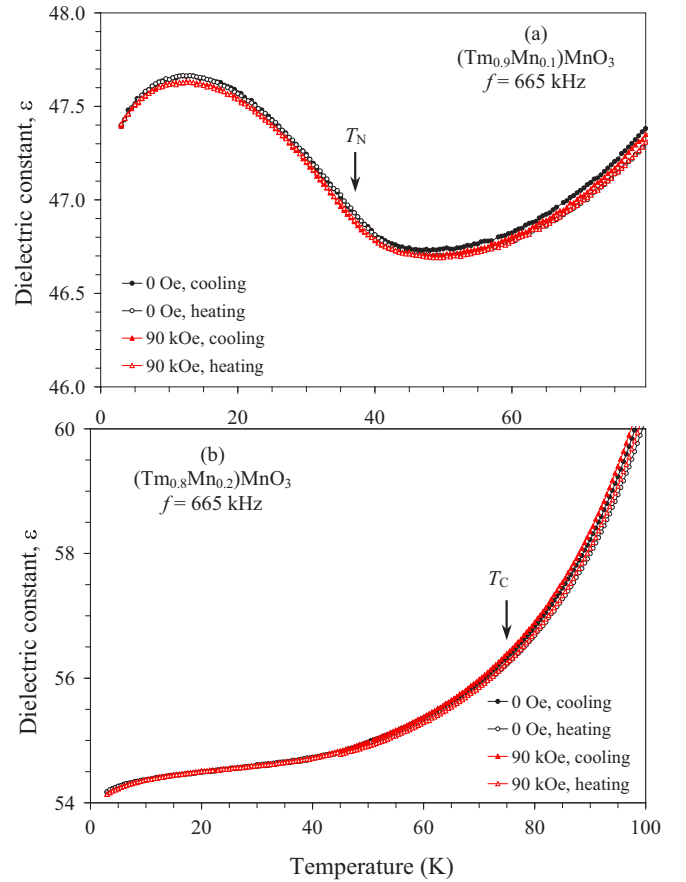


FIG. 18. Temperature dependence of dielectric constant in (a) $(\text{Tm}_{0.9}\text{Mn}_{0.1})\text{MnO}_3$ and (b) $(\text{Tm}_{0.8}\text{Mn}_{0.2})\text{MnO}_3$. Measurements were performed on cooling (filled symbols) and heating (empty symbols) at $H = 0$ Oe (black) and 90 kOe (red). The data at one frequency of 665 kHz are shown.

sizes) at the A site causes significant microstrain effects along the a direction which are absent in o-TmMnO_3 and get stronger with increasing doping of Mn^{2+} . Ordering of magnetic Mn moments triggers short-range order (for $x = 0.1$) and long-range order (for $x \geq 0.2$) of the Tm^{3+} cations at the same temperature—an unusual situation in perovskite materials with a simple GdFeO_3 -type $Pnma$ structure. For $x = 0.1$, long-range IC order of magnetic Mn moments at the B site coexists with short-range order of Tm^{3+} and Mn^{2+} moments at the A site. Short-range order is induced at the Néel temperature $T_N = 37$ K, increases towards an additional specific heat anomaly at $T = 4$ K, and remains at lower temperature. The magnetic structure of $(\text{Tm}_{0.9}\text{Mn}_{0.1})\text{MnO}_3$ is different from that of the parent compound o-TmMnO_3 [7], which further evolved into an E -type commensurate magnetic structure with the appearance of spin-induced ferroelectricity. For $0.2 \leq x \leq 0.3$, a ferrimagnetic structure is stabilized below $T_C = 75$ K ($x = 0.2$) and $T_C = 104$ K ($x = 0.3$) with the appearance of negative magnetization effects below a compensation temperature of about 15 K. Our magnetic structure determination could clarify the mechanism of negative magnetization effects as the different temperature evolution of sublattice magnetizations—a classical mechanism proposed by Néel for N -type ferrimagnets [36].

ACKNOWLEDGMENTS

This work was partly supported by JSPS KAKENHI Grant No. JP16H04501, a research grant from Nippon Sheet Glass Foundation for Materials Science and Engineering (40-37),

and Innovative Science and Technology Initiative for Security, ATLA, Japan. This work is partially based on experiments performed on HRPT diffractometer (Proposal No. 20180113) at the Swiss Spallation Neutron Source SINQ, Paul Scherrer Institut, Switzerland.

-
- [1] R. H. Mitchell, in *Perovskites: Modern and Ancient* (Almaz, Thunder Bay, Ontario, Canada, 2002).
- [2] A. M. Abakumov, A. A. Tsirlin, and E. V. Antipov, Transition-Metal Perovskites, in *Comprehensive Inorganic Chemistry II (Second Edition): From Elements to Applications*, edited by J. Reedijk and K. R. Poeppelmeier (Elsevier, Amsterdam, 2013), Vol. 2, p. 1.
- [3] E. Bousquet and A. Cano, *J. Phys.: Condens. Matter* **28**, 123001 (2016).
- [4] M. Tachibana, T. Shimoyama, H. Kawaji, T. Atake, and E. Takayama-Muromachi, *Phys. Rev. B* **75**, 144425 (2007).
- [5] A. Kumar, S. M. Yusuf, and C. Ritter, *Phys. Rev. B* **96**, 014427 (2017).
- [6] A. Munoz, M. T. Casais, J. A. Alonso, M. J. Martínez-Lope, J. L. Martínez, and M. T. Fernández-Díaz, *Inorg. Chem.* **40**, 1020 (2001).
- [7] V. Y. Pomjakushin, M. Kenzelmann, A. Dönni, A. B. Harris, T. Nakajima, S. Mitsuda, M. Tachibana, L. Keller, J. Mesot, H. Kitazawa, and E. Takayama-Muromachi, *New J. Phys.* **11**, 043019 (2009).
- [8] A. A. Belik and W. Yi, *J. Phys.: Condens. Matter* **26**, 163201 (2014).
- [9] M. Markkula, A. M. Arevalo-Lopez, A. Kusmartseva, J. A. Rodgers, C. Ritter, H. Wu, and J. P. Attfield, *Phys. Rev. B* **84**, 094450 (2011).
- [10] A. J. Dos Santos-Garcia, C. Ritter, E. Solana-Madruga, and R. Saez-Puche, *J. Phys.: Condens. Matter* **25**, 206004 (2013).
- [11] A. M. Arevalo-Lopez, F. Stegmann, and J. P. Attfield, *Chem. Commun.* **52**, 5558 (2016).
- [12] M. R. Li, M. Retuerto, Z. Deng, P. W. Stephens, M. Croft, Q. Huang, H. Wu, X. Deng, G. Kotliar, J. Sánchez-Benítez, J. Hadermann, D. Walker, and M. Greenblatt, *Angew. Chem., Int. Ed.* **54**, 12069 (2015).
- [13] A. M. Arévalo-López, G. M. McNally, and J. P. Attfield, *Angew. Chem., Int. Ed.* **54**, 12074 (2015).
- [14] A. N. Vasil'ev and O. S. Volkova, *Low Temp. Phys.* **33**, 895 (2007).
- [15] R. D. Johnson, D. D. Khalyavin, P. Manuel, P. G. Radaelli, I. S. Glazkova, N. Terada, and A. A. Belik, *Phys. Rev. B* **96**, 054448 (2017).
- [16] R. D. Johnson, D. D. Khalyavin, P. Manuel, L. Zhang, K. Yamaura, and A. A. Belik, *Phys. Rev. B* **98**, 104423 (2018).
- [17] J. Sánchez-Benítez, J. A. Alonso, A. de Anres, M. J. Martínez-Lope, J. L. Martínez, and A. Munoz, *Chem. Mater.* **17**, 5070 (2005).
- [18] L. Zhang, N. Terada, R. D. Johnson, D. D. Khalyavin, P. Manuel, Y. Katsuya, M. Tanaka, Y. Matsushita, K. Yamaura, and A. A. Belik, *Inorg. Chem.* **57**, 5987 (2018).
- [19] A. A. Belik, *Dalton Trans.* **47**, 3209 (2018).
- [20] A. M. Vibhakar, D. D. Khalyavin, P. Manuel, L. Zhang, K. Yamaura, P. G. Radaelli, A. A. Belik, and R. D. Johnson, *Phys. Rev. B* **99**, 104424 (2019).
- [21] E. Solana-Madruga, A. M. Arevalo-Lopez, A. J. Dos Santos-Garcia, E. Urones-Garrote, D. Avila-Brandé, R. Saez-Puche, and J. P. Attfield, *Angew. Chem. Int. Ed.* **55**, 9340 (2016).
- [22] E. Solana-Madruga, A. M. Arévalo-López, A. J. Dos Santos-Garcia, C. Ritter, C. Cascales, R. Sáez-Puche, and J. P. Attfield, *Phys. Rev. B* **97**, 134408 (2018).
- [23] L. Zhang, D. Gerlach, A. Dönni, T. Chikyow, Y. Katsuya, M. Tanaka, S. Ueda, K. Yamaura, and A. A. Belik, *Inorg. Chem.* **57**, 2773 (2018).
- [24] L. Zhang, A. Dönni, V. Y. Pomjakushin, K. Yamaura, and A. A. Belik, *Inorg. Chem.* **57**, 14073 (2018).
- [25] A. Kumar and S. M. Yusuf, *Phys. Rep.* **556**, 1 (2015).
- [26] P. Fischer, G. Frey, M. Koch, M. Könnecke, V. Pomjakushin, J. Schefer, R. Thut, N. Schlumpf, R. Bürge, U. Greuter, S. Bondt, and E. Berruyer, *Physica B* **276–278**, 146 (2000).
- [27] J. Rodríguez-Carvajal, *Physica B* **192**, 55 (1993).
- [28] R. Rodríguez-Carvajal, M. T. Fernández-Díaz, and J. L. Martínez, *J. Phys.: Condens. Matter* **3**, 3215 (1991).
- [29] P. W. Stephens, *J. Appl. Crystallogr.* **32**, 281 (1999).
- [30] N. E. Brese and M. O'Keeffe, *Acta Crystallogr. Sect. B* **47**, 192 (1991).
- [31] K. Momma and F. Izumi, *J. Appl. Crystallogr.* **244**, 1272 (2011).
- [32] T. Hahn, in *International Tables for Crystallography, Volume A, Space Group Symmetry (Fifth Edition)* (Wiley, New York, 2005).
- [33] D. B. Litvin, in *Magnetic Group Tables* (International Union of Crystallography, Chester, England, 2013); www.iucr.org/pub/978-0-9553602-2-0.
- [34] K. Uusi-Esko, J. Malm, N. Imamura, H. Yamauchi, and M. Karppinen, *Mater. Chem. Phys.* **112**, 1029 (2008).
- [35] See Supplemental Material at <http://link.aps.org/supplemental/10.1103/PhysRevB.101.054442> for more details on magnetic properties.
- [36] L. Néel, *Ann. Phys. (Paris)* **12**, 137 (1948).